Volcanism on Io: A Comparison Between the Volcanic Distribution and Tidal Stress

Master of Science Thesis

Duncan van Sliedregt 4462106

Supervisors Teresa Steinke Wouter van der Wal

Date of Delivery May 26, 2020

Delft University of Technology

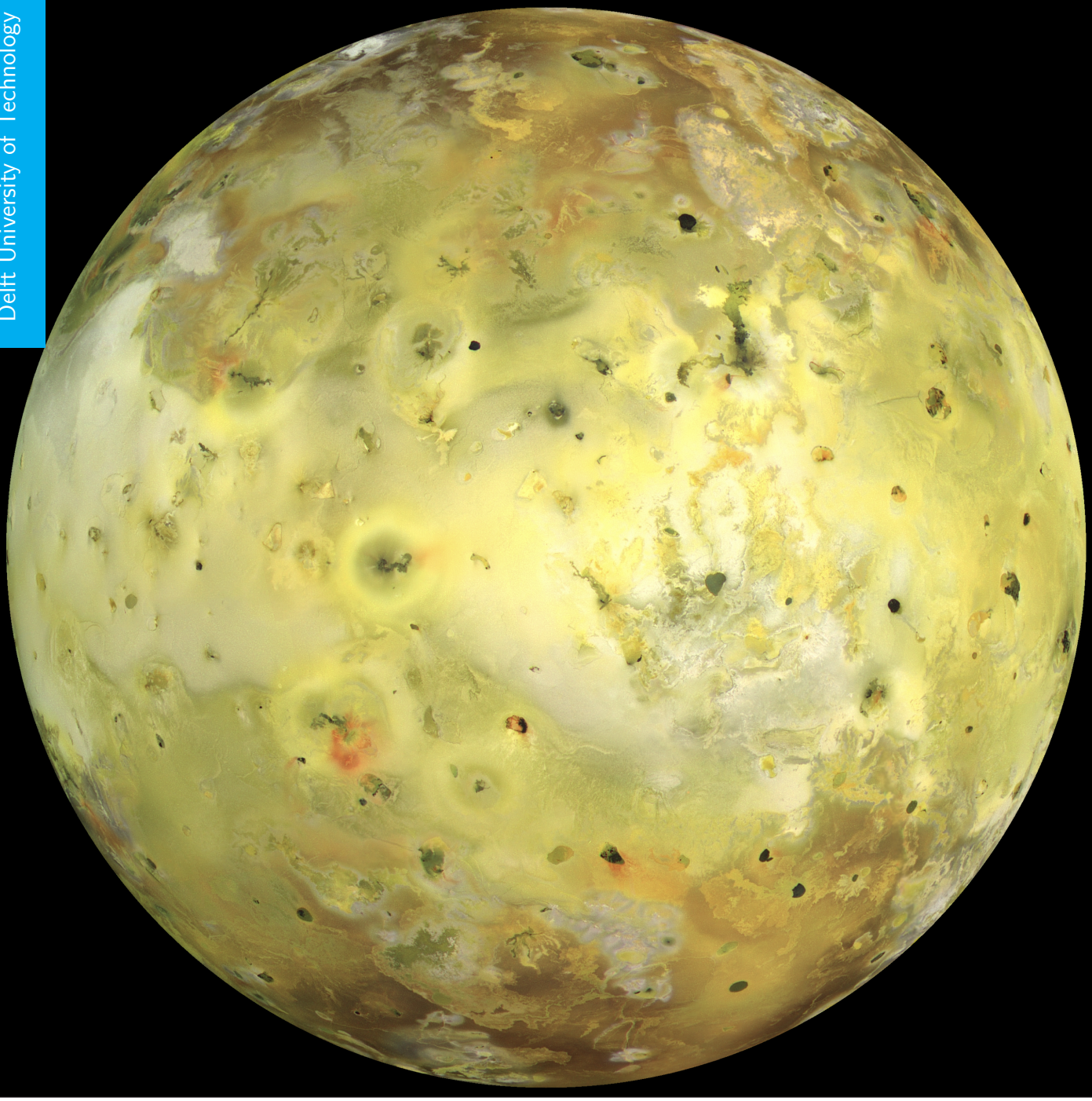

TU Delft Delft University of Technology

Challenge the future

Cover: A true color image of Jupiter's moon Io, taken on 3 July 1999 at a range of about 130,000 kilometers by NASA's Galileo spacecraft.

Credit: Galileo, NASA's first Jupiter Orbiter

ABSTRACT

Io is Jupiter's innermost Galilean satellite and the most volcanically active body in the Solar System. Its volcanism is driven by tidal heating generated by its interaction with Jupiter and maintained by the Galilean satellites, Europa and Ganymede. The tidal forces acting on Io also cause significant stresses on its interior. Heat is transferred to the surface through the advection of magma via heat-pipes in the lithosphere (O'Reilly and Davies, 1981). Therefore, by studying the distribution of Io's volcanic centers, insight into its interior processes can be gained.

The purpose of this thesis is to investigate the hypothesis that tensional stresses play a significant role in the formation of volcanic centers on Io. This is analogous to Earth, where tensile stresses are thought to cause intraplate volcanism (Turcotte and Oxburgh, 1976). To test the hypothesis, the stress and volcanism are examined on a local and global scale. On a global scale, it is investigated if the locations of maximum tensile stress coincide with the locations of maximum volcanic activity. While on a local scale, it is investigated if potential chains of Io's volcanoes follow the directions of the tensile stresses.

Observations of volcanic centers from multiple sources are combined and filtered to form a single data set. This data set contains a volcanic distribution consisting of 794 volcanic centers with near-global coverage of Io's surface. A statistical analysis is performed on this volcanic distribution. The global-scale analysis is accomplished using a spherical harmonic analysis. This method shows where volcanic centers are concentrated and at which wavelength. The analysis of Io's volcanic distribution showed a statistically significant degree 2 signal centered around the equator with a 30 degree eastward offset from the tidal axis. The local-scale analysis is performed using a specially developed curve reconstruction algorithm. This algorithm allows for determining local connections between volcanoes, such as chains of volcanoes and their directions. Unlike on Earth, no significant amount of chains were found on Io. However, the chains that were found showed potential alignment.

The diurnal tidal stresses on Io are determined analytically. The diurnal stresses are dependent on Io's tidal response, which is determined using a four-layer model of Io's interior. This model of Io's interior is based upon the asthenospheric heating model of Segatz et al. (1988). The tensile stresses used in the comparison between stress and volcanism are defined along the principal axes.

To determine if the results of the analyses performed in this thesis are statistically significant, Monte Carlo analyses were performed. These analyses were performed using randomly distributed and clustered randomly distributed data sets. The clustered data set is included to simulate the statistically significant spatial clustering of volcanoes in Io's volcanic distribution.

On a local scale, it was found that there is a statistically significant alignment between the direction of the tensile stress and the direction of the volcanic chains roughly 30 degrees before apojove. This significant alignment deviates from a random distribution of volcanic centers and cannot be attributed to the clustering of volcanic centers. On a global scale, it was found that there is a significant correlation between the degree 2 spherical harmonics of the tensile stress field and the volcanic distribution. This correlation can, however, be attributed to a random distribution and outliers of a clustered distribution. Similar to the local scale results, the global scale results have a 30 degree offset with respect to the apsides. This offset cannot be attributed to a potential magma ocean but could be attributed to a faster-than-synchronous rotation.

Overall, the results on a global and local scale are shown to be consistent with the hypothesis that tensional stresses play a significant role in the formation of volcanic centers on Io. However, tensional stresses alone are not sufficient for the formation of volcanic centers.

LIST OF FIGURES

LIST OF TABLES

CONTENTS

1

INTRODUCTION

Jupiter's moon Io is the most volcanically active body in the Solar System. This immense volcanism is the byproduct of the dissipation of tidal energy (Peale et al., 1979) from its orbit around Jupiter. This is different from Earth, which is predominantly heated by radiogenic sources (Turcotte and Schubert, 2002). Io is caught in an orbital resonance with Europa and Ganymede. This orbital resonance is known as the Laplace resonance and forces Io's orbit to be slightly eccentric (Segatz et al., 1988), which helps drive the tidal dissipation (Peale et al., 1979). Io's interior processes are not yet fully understood. By better understanding these processes on Io, insight into similar processes, e.g. tidal heating, on other moons can be gained. This could help predict the presence of liquid water on moons such as Enceladus or Europa (de Kleer and de Pater, 2016), and could even help predict volcanism or liquid water on exoplanets (de Kleer and de Pater, 2016; Henning et al., 2018).

On Io one of the interior processes, tidal heating, presents itself on the surface through volcanism (de Kleer and de Pater, 2016). Io has a mean global heat flow of approximately 2.24 W m^{-2} (Lainey et al., 2009), roughly 20 times larger than that of Earth (Turcotte and Schubert, 2002). This heat is primarily transported to the surface by silicate volcanism (McEwen et al., 2004). Over 500 unique volcanic centers, defined as the source where the volcanic material originates (Schenk et al., 2001), have been found spread out over Io's surface. One of these volcanic centers, Loki Paterae, is by far the most powerful example of the immense volcanism, producing roughly 25% of Io's total global heat flow (Moore et al., 2007). As the volcanic activity is representative of Io's global heat flow, studying the distribution of the volcanic centers can constrain models of its interior structure and processes (Hamilton et al., 2013).

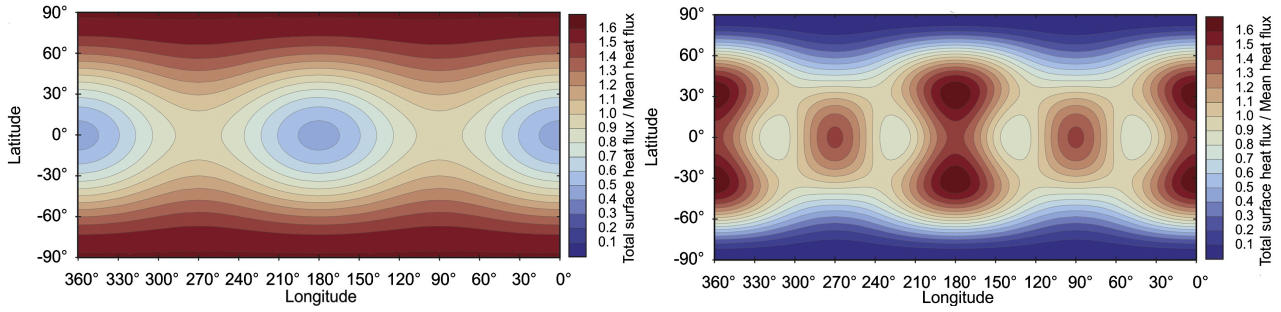

(a) (b)

Figure 1.1: Contours of Io's surface heat flow due to tidal dissipation for (a) the deep-mantle heating end-member model and (b) the asthenospheric heating end-member model. Images were obtained from Hamilton et al. (2013).

To support Io's immense heat flow, two end-member models for Io's interior have been developed, the deep mantle model and the asthenosphere model (Segatz et al., 1988). Mixed models also exist, combining the different mechanisms of two heating models.

As the name suggests, in the first model the majority of the dissipation occurs within the mantle. As illustrated in Figure 1.1a, the surface heat flow is at a maximum near the poles and is at a minimum near the equator. In the second model, a thin partially molten asthenosphere separates the mantle from the lithosphere. Tidal heating occurs primarily within this asthenosphere.

As illustrated in Figure 1.1b, this model predicts the surface heat flow to be at a minimum near the poles and at a maximum near the equator. Specifically, the primary maxima occur near the north and south of the subjovian and antijovian points, with secondary maxima occurring at the centers of the leading and trailing hemispheres.

It is often assumed that the locations of the volcanic centers are directly correlated to the surface heat flow (Hamilton et al., 2013), with dissipation patterns such as in the two-end member models. Regions of higher heat flux would then result in more volcanic activity.

The surface of Io supports some of the tallest and steepest mountains in the Solar System. For a lithosphere to exist that can support these mountainous features, as well as support the tremendous volcanic activity, a heat-pipe mechanism has been suggested by O'Reilly and Davies (1981). The heat-pipe mechanism works by means of melt transport through fissures in a thicker lithosphere. The most important implication of this mechanism is that as eruptions spread material across the surface, they bury old material (O'Reilly and Davies, 1981). This implies a global resurfacing of Io, at a rate of 1-2cm per year (O'Reilly and Davies, 1981; Moore et al., 2007).

The heat-pipe mechanism is also used to gain insight into the thickness of the asthenosphere. Using a melt fraction of 10-20%, Moore et al. (2007) estimated the asthenosphere to be between 60-120 km thick. This matches the study by Khurana et al. (2011). Using magnetometer data collected by the Galileo spacecraft, Khurana et al. (2011) found evidence of a partially molten asthenosphere of at least 50 km thick, with a melt fraction of approximately 20%.

Several studies have performed statistical analyses of Io's volcanic distribution (e.g. Hamilton et al., 2013; Kirchoff et al., 2011; de Kleer and de Pater, 2016).

It was found that regions on Io showed significant spatial clustering of volcanic centers. Clustering may indicate that multiple volcanic centers are fed from the same sources at great depths or it may be indicative of mantle plume volcanism (Hamilton et al., 2013; Ernst and Desnoyers, 2004; Connor et al., 2000). the clustering of volcanic centers can be caused by several phenomena. Clustering can occur due to multiple volcanic centers forming near longer-lived hot-spots that are fed from greater depths, sharing the same magma source (Hamilton et al., 2013). Similarly, clustering could also occur if multiple volcanic centers were being fed from one magma reservoir (Garcia et al., 2003). On Venus, mantle plumes are thought to occur in clusters causing regional concentrations of volcanism (Ernst and Desnoyers, 2004). This mechanism could also be responsible for the volcanic clustering on Io.

Kirchoff et al. (2011), and Hamilton et al. (2013) found that the volcanic distribution implies the asthenospheric heating model, but with a 30-60° eastward offset. This offset can be caused by a state of stress controlling the locations of the volcanic centers, a faster-than-synchronous rotation, and/or a missing component in Io's tidal response. Tyler et al. (2015) developed a model of Io's interior, using a magma ocean that can explain the observed eastward offset of the volcanic distribution.

Io's eccentric orbit causes it to go through a cycle of expansion and contraction as it orbits around Jupiter. This cycle causes stress in the lithosphere (Bart et al., 2004). The expansion causes tensile stresses, while the contraction results in compressive stresses.

Tidal stresses have also been thought to be the cause of surface features on other Galilean moons. Tidal stresses are thought to explain the formation of the characteristic lineae on Europa's surface (Jara-Orué and Vermeersen, 2011) and stresses on Ganymede are thought to be great enough to induce Coulomb failure and generate strike-slip faults (Cameron et al., 2019). The surface of Io is rapidly resurfaced. As a result, tectonic faults may not be visible. However, volcanic centers may indicate if and where these faults exist. On Earth, Turcotte and Oxburgh (1976) proposed that intraplate volcanism can be attributed to the tensional fracturing of the lithosphere. Stresses in the lithosphere accumulate over geological time scales, these accumulated stresses then cause fractures in the lithosphere, allowing volcanism to occur. Solomon (1978) proposes

a similar mechanism for one-plate bodies, such as Mars and the Moon. Solomon (1978) also states that magma transport is greatly aided by tensional stresses.

As Io does not have active plate tectonics (McEwen et al., 2004; Schenk et al., 2001) and undergoes significant tensile tidal stresses, the objective of this thesis is to test the hypothesis that *tensional stresses play a significant role in the formation of volcanic centers on Io.*

To investigate this hypothesis, stress and volcanism are examined on a local and a global scale. This approach leads to two sub-hypotheses. First, on a local scale, it is investigated if chains of Io's volcanoes follow the direction of the tensile stresses. If chains of volcanoes are aligned with the direction of the tensile stresses, it could suggest that volcanic eruptions are propagated through stress-induced fractures in the lithosphere. Second, on a global scale, if the locations of maximum tensile stress coincide with the locations of maximum volcanic activity. If areas of maximum stress coincide with areas of maximum volcanic activity, it could suggest that volcanism in these regions can be attributed to fractures in the lithosphere.

This thesis is structured in the following way. First, Chapter 2 discusses the statistical analysis of the spatial distribution of Io's volcanic centers is performed. The data set of the volcanic distribution is obtained by combining multiple data sets from different sources for a more complete global coverage. The statistical analysis for the quantification of Io's volcanic distribution for comparison to the tensile stress. Second, Chapter 3 discusses the diurnal stresses on Io and the tensile component of its principal axes. The tensile stresses and the volcanic distribution are compared on a local and global scale in Chapter 4. This comparison will also investigate if a state of stress can control the location of volcanism and can cause the observed 30-60° eastward offset in the volcanic distribution. Next, Chapter 5 discusses the most significant results from the previous comparison. Finally, Chapter 6 serves as a conclusion and presents recommendations for future work.

2
STATISTICAL ANALYSIS

This chapter focuses on the statistical analysis of the spatial distribution of Io's volcanic centers. To determine the link between the tensile stress and volcanism, the locations of the volcanic centers, how they are spaced relative to each other, and if they form patterns must first be understood.

This chapter is divided into three sections. First, the data on the locations of volcanic centers are selected and filtered. Second, the method of generating completely random, and slightly clustered but random, volcanic distributions is introduced. These random distributions will be used to perform Monte Carlo analyses to investigate the significance of Io's volcanic distribution with the aim to identify if the underlying physical processes are present. Next, a spherical harmonic analysis is performed, this allows for examining the spatial distribution on a global scale. Finally, a curve reconstruction algorithm is used to determine the local connections between volcanic centers, such as how the volcanoes organized.

2.1. DATA SET

This section is split into three parts. First, the different data sources are discussed, along with how the data was obtained. Second, the data is filtered to remove any duplicate volcanic centers. Finally, the observational coverage of the filtered volcanic distribution is discussed.

2.1.1. SELECTION OF OBSERVATIONS

For the data analysis in this chapter, multiple data sets of volcanic centers were used. Multiple data sources were used to improve the observational coverage as well as to ensure the quality of the results. This analysis will make use of the data obtained from Davies et al. (2015), Hamilton et al. (2013), Mura et al. (2020), and de Kleer et al. (2019). The volcanic centers from these data sets are illustrated in Figure 2.1.

The data obtained from Davies et al. (2015) is a collection of 250 volcanic centers, a combination of paterae and hot spots. Most of the volcanic centers in this data set are determined from data gathered by the Galileo spacecraft's Near Infrared Mapping Spectrometer (NIMS) and Photo-Polarimeter Radiometer (PPR) instruments (Davies et al., 2015; Veeder et al., 2015). The NIMS and PPR instruments have a typical spatial resolution of 150-300 km/pixel and 250-300 km/pixel, respectively. Unfortunately, Galileo only managed direct observational coverage of Io's equatorial area, not its poles (Davies et al., 2015). Several other volcanic centers in this data set were observed using multi-wavelength infrared radiometry from Earth-based adaptive optics telescopes (Marchis et al., 2000; de Kleer et al., 2014; de Pater et al., 2014) and other spacecraft that flew by Jupiter, i.e. Voyager, New Horizons and Cassini (Veeder et al., 2012). These methods have a variety of spatial resolutions, between 61 km/pixel for Cassini, 700 km/pixel for Voyager, and up to 1800 km/pixel for the Infrared Telescope Facility. The spacecraft all did fly-bys and therefore did not have the opportunity to provide significant coverage. Similarly, the Earth-based telescopes only contributed a handful of volcanic centers.

The second data set was obtained from Hamilton et al. (2013) and is made up of 173 hot spots and 529 paterae. This data set is based on data collected by the Voyager, Galileo, and New Horizons spacecraft, and, similarly to that of Davies et al. (2015), is supplemented by observations from Earth-based telescopes (Hamilton et al., 2013; Spencer et al., 2007; Lopes and Spencer, 2007).

The list of paterae is obtained from a 1 km/pixel reprocessed map of the Voyager-Galileo mosaic (Becker and Geissler, 2005). However, in the original data from Galileo and Voyager only 83% of Io's surface was imaged at a spatial resolution of 5 km/pixel or better Hamilton et al. (2013). Thus, the reprocessed mosaic still contains the same observational biases as with the data set by Davies et al. (2015).

The third data set was obtained from Mura et al. (2020) using the Jovian InfraRed Auroral Mapper (JIRAM) instrument aboard the Juno spacecraft. Due to the Juno spacecraft's inclined and eccentric orbit, unprecedented coverage of Io's poles was achieved at a higher resolution than Galileo's NIMS instrument. This allowed for the observation of unseen volcanic eruptions at higher latitudes (Mura et al., 2020).

The last data set was obtained from de Kleer et al. (2019). As opposed to the previous data sets, this data set was exclusively obtained via Earth-based adaptive optics telescopes. This allowed for more continuous monitoring of Io's volcanic activity over a period of 271 nights between 2013 and 2018. During this period, over 980 volcanic eruptions were observed from at least 85 unique volcanic centers (de Kleer et al., 2019). The spatial resolution of this method is comparable to that of the typical NIMS observation. Similarly, this method does not yield good coverage of Io's poles (de Kleer et al., 2019).

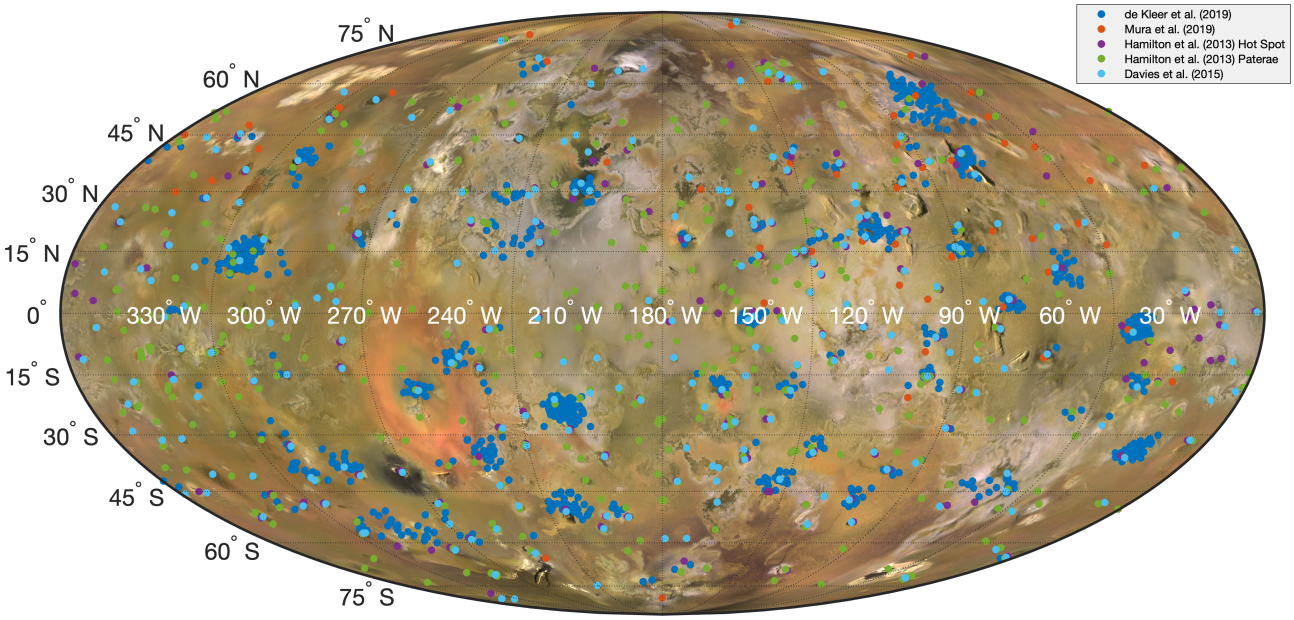

Figure 2.1: All 1982 volcanic centers from the data sets from Davies et al. (2015), Hamilton et al. (2013), Mura et al. (2020), and de Kleer et al. (2019). The background image is a Mosaic of Io obtained from USGS (2012).

2.1.2. Filtering

The four different data sets were compiled over a large period of time, as well as using different observation techniques. This has lead to a significant overlap between the data sets and therefore the data sets must be filtered to remove any potential duplicate volcanic center before one combined data set can be compiled. The aim of the combining of the data sets is to produce a final data set with the best coverage of volcanic centers and the least amount of possible overlap between sources. This sample of volcanic centers in the data set can then be representative of Io's global volcanic distribution. Another consequence of gathering data over a large period of time is that surface features can change during this time (Rathbun et al., 2014; Geissler et al., 2004). Changes in surface features could also see that older volcanic centers may disappear and new volcanic centers may pop up. However, this should not influence the conclusion as the location of older volcanic centers is still relevant to understanding the mechanism behind their formation.

The filtering process is split up into three parts and is discussed in the upcoming paragraphs. First, the de Kleer et al. (2019) and Mura et al. (2020) data sets are filtered. These two are combined as the standard deviations in the location are known. Second, the overlap between the data sets without standard deviations, Hamilton et al. (2013), and Davies et al. (2015), are filtered out. Finally, all four filtered data sets are compiled into one final data set.

First, the de Kleer et al. (2019) and Mura et al. (2020) data sets are filtered. The de Kleer et al. (2019) data set contains 980 eruptions, most of these are of the same volcanic centers. This is due to the, previously mentioned, time frame over which the data points were collected. As this data set was obtained solely from Earth-based telescopes, there are significant deviations in the locations of the eruptions. Similarly, the 50 eruptions in the data set from Mura et al. (2020), obtained using the JIRAM data, also contains significant deviations in the locations. The standard deviations for the longitude and latitude of the volcanic centers are supplied by Mura et al. (2020) and de Kleer et al. (2019). These standard deviations, at a 3-sigma or 99% confidence interval, are used to filter out the potential duplicates.Figure 2.2 illustrates two observed eruptions with their longitudinal and latitudinal uncertainties plotted as ellipses. To ensure that no duplicate volcanic centers are in this combined data set, it is assumed that the overlapping eruptions occur from the same volcanic center. This is achieved by removing the volcanic center with the highest uncertainty. This first filtering step leaves 162 unique volcanic centers out of 1030 observations of the combined de Kleer et al. (2019) and Mura et al. (2020) data sets.

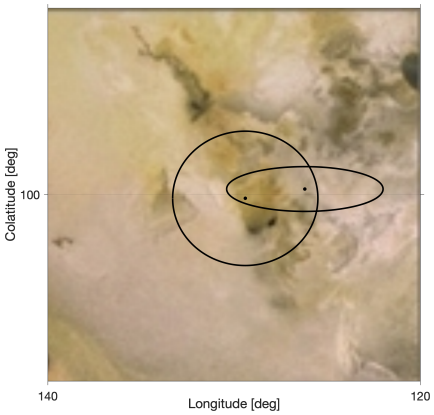

Figure 2.2: Two volcanic centers from de Kleer et al. (2019) with overlapping 3-sigma uncertainties.

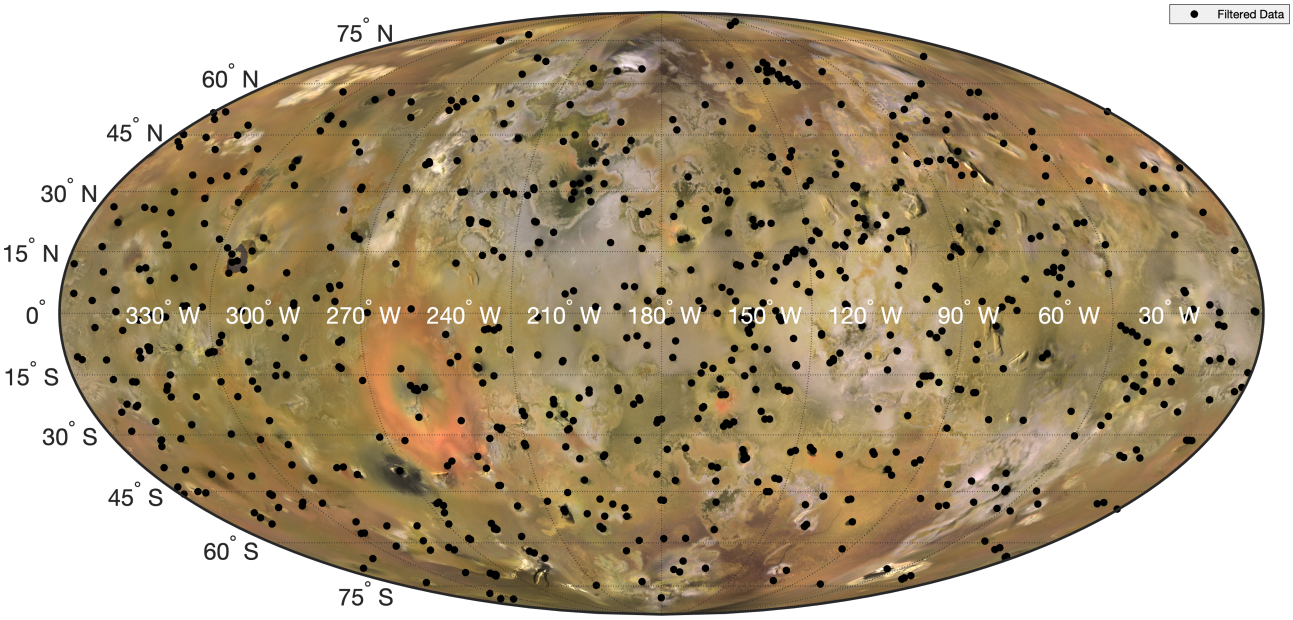

Figure 2.3: The filtered data set of 794 volcanic centers obtained from filtering the data sets from Davies et al. (2015), Hamilton et al. (2013), Mura et al. (2020), and de Kleer et al. (2019). The background image is a Mosaic of Io obtained from USGS (2012).

Next, the overlapping volcanic centers from the Hamilton et al. (2013) and Davies et al. (2015) data sets are removed. Paterae in both sets of data are obtained using similar data sources (e.g. the Galileo NIMS and PPR data). However, different processing techniques result in slight variances in the locations of the same paterae. To remove duplicates due to this variance, a simple check is performed using the location and supplied area of the patera. First, the distance between the paterae

is calculated. Second, the effective radii of the paterae are determined. The effective radius, r_e, is the radius assuming the patera is circular, $A = \pi r_e^2$. Finally, if the distance between the paterae is less than each of their respective effective radii, it is assumed that they are the same patera. After filtering out the duplicate paterae from Hamilton et al. (2013) and Davies et al. (2015), the 173 hot spots from Hamilton et al. (2013) are examined. According to Hamilton et al. (2013), almost two-third of these hot spots are located within the paterae in their data set. This implies that the hot spots are active paterae and also need to be filtered. This is done by determining if a hot spot is located within a patera. If this is the case, the patera is removed from the filtered paterae data set. This significantly decreases potential duplicate volcanic centers within the distribution. The filtering of the hot spots and paterae leaves 678 unique volcanic centers out of 952 observations of the combined Hamilton et al. (2013) and Davies et al. (2015) data sets.

Finally, the 162 volcanic centers from the first filtering step are combined with the 678 volcanic centers from the second filtering step.

As both sets contain volcanic centers such as Loki patera, the largest and most powerful volcanic center on Io (de Kleer and de Pater, 2016; Rathbun et al., 2004), duplicates between these two data sets must be removed as well. This is done by determining if any of the 678 volcanic centers from the combined Davies et al. (2015) and Hamilton et al. (2013) data set fit within the 3-sigma confidence interval of the 162 volcanic centers from the combined de Kleer et al. (2019) and Mura et al. (2020) data set. If there is any overlap between the two data sets, the volcanic center from the combined de Kleer et al. (2019) and Mura et al. (2020) data set is removed. The volcanic center from this data set is removed due to it having a significant deviation in location as opposed to that of the Davies et al. (2015) and Hamilton et al. (2013) data set. After removing any remaining duplicates between the two sets, a data set of 794 volcanic centers remains. Although, volcanic centers may be removed from the data set that are not duplicates. It is assumed that, due to the relatively small number of volcanic centers removed in this step in combination with the fact that volcanic centers such as Loki patera occur in both data sets, that the all overlapping volcanic centers are duplicates. The final 794 volcanic centers from this data set are illustrated in Figure 2.3.

2.1.3. Observational Coverage

As previously mentioned, multiple data sets are used in this analysis in order to ensure complete coverage of Io's surface. The data obtained from Davies et al. (2015) shows a large number of volcanic centers near a region located between $90°W - 180°W$ and $45°S - 45°N$. This may be biased due to the high spatial resolution data collected by Galileo of this region Davies et al. (2015). Similarly, the data collected by Hamilton et al. (2013) indicates data with a lower spatial resolution between $0°W - 90°W$, and above $60°N$ and below $75°S$. The data sets from Davies et al. (2015), Hamilton et al. (2013), and de Kleer et al. (2019) lack observations of Io's polar regions. Contrary to this, the data collected by Juno and analyzed by Mura et al. (2020) had good coverage of Io's polar regions. As mentioned, this is due to Juno's inclined and eccentric orbit around Jupiter.

Similar to Hamilton et al. (2013), it is assumed that the determined volcanic distribution is representative of Io's global volcanic distribution. The accuracy of this distribution is greatly increased due to the significant increase of the observational coverage of Io's poles with the addition of Juno's JIRAM data, in combination with the average size of the volcanic centers combined with the spatial resolution of the different sources.

To visually represent the observational coverage of the combined filtered data set, a pair of histograms are plotted in Figure 2.4. As can be seen in this figure, the combined data contains few volcanic centers near the poles, a peak between $90°W - 180°W$, and a relative dearth of volcanic centers between $0°W - 90°W$. This is consistent with the previously mentioned observations (Hamilton et al., 2013; Mura et al., 2020; de Kleer et al., 2019; Davies, 2007).

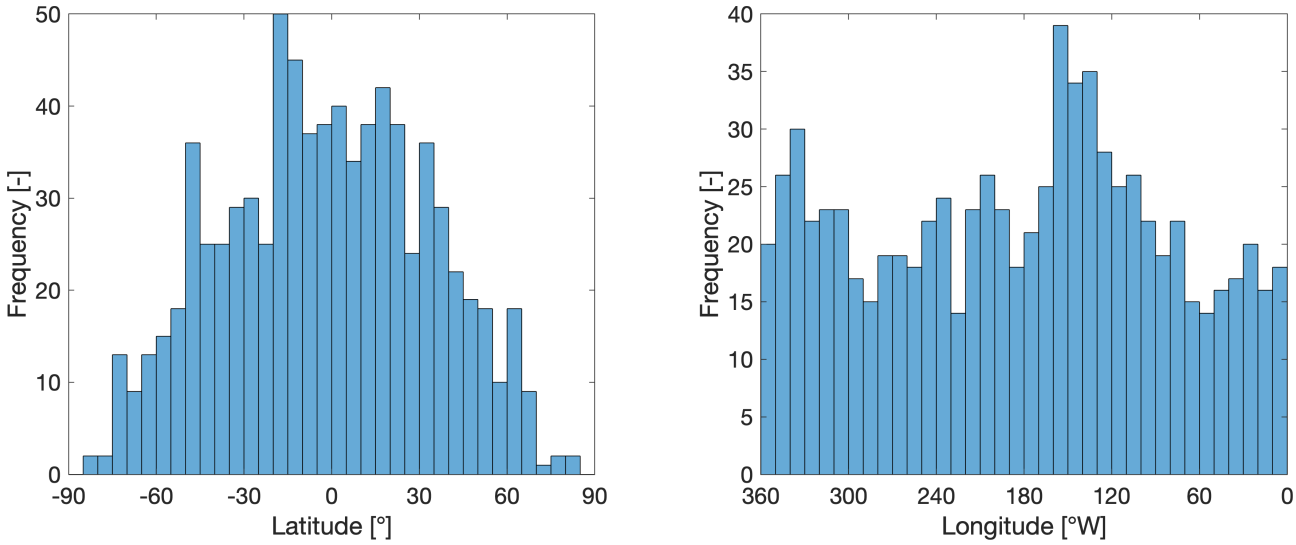

Figure 2.4: Histograms of the spatial distribution of the latitude (left) and longitude (right) of the 794 filtered volcanic centers. The bin size is equal to 5° (left) and 10° (right).

2.2. Monte Carlo Analysis

To test if the tensional stresses are indeed responsible for Io's volcanism, Monte Carlo analyses are performed using random and clustered random distribution. Volcanic centers that are clustered are more closely spaced together than would be expected for a true random distribution. This section introduces the methods of generating sample distributions that are used.

First, the method of generating random distributions on a sphere is introduced. If analyses using Io's volcanic distribution match that of a random distribution, it may indicate that the volcanic centers formed independently of each other (Hamilton et al., 2013).

Second, the method of generating random distributions that mimic the clustered behavior of Io's volcanic distribution is introduced. If the analyses using Io's volcanic distribution match that of a clustered random distribution, it may indicate that the clustering of volcanic centers plays a significant role in their formation. It also allows for removing the influence of clustering from Io's volcanic distribution allowing for further investigating of the significance of the distribution.

2.2.1. Random Distribution

This section introduces the equations used for generating a random distribution of points on a sphere. For each point, a colatitude and longitude coordinate are generated. The colatitude is weighted in order to compensate for the smaller area at higher latitudes. This weighting removes biases towards higher latitudes by equalizing the probability over the entire globe. A random distribution is generated using the following equations:

$$\theta = \arcsin\left(2U(N) - 1\right) + 90° \tag{2.1}$$

$$\phi = 360U(N) \tag{2.2}$$

where θ is the colatitude, ϕ is the longitude, and $U(N)$ are N number of uniform random variables between 0 and 1 (Hamilton et al., 2013).

2.2.2. Clustered Random Distribution

This section introduces the algorithm used to generate a clustered random distribution of points on a sphere. A clustered random distribution is an oxymoron, as a distribution that is spatially clustered cannot be not truly randomly distributed. For this thesis, a clustered random distribution is a distribution with arbitrarily determined volcanic clusters combined with randomly

placed non-clustered volcanic centers. As mentioned, if the analyses using Io's volcanic distribution match that of a clustered random distribution, it may indicate that the clustering of volcanic centers plays a significant role in their formation. The clustering of volcanic centers may indicate that multiple volcanic centers are fed from the same sources at great depths or it may be indicative of mantle plume volcanism (Hamilton et al., 2013; Ernst and Desnoyers, 2004; Connor et al., 2000).

To determine the degree of clustering for the sample distribution, the degree of clustering for Io's volcanic distribution must first be determined. This is done by using the Nearest Neighbor (NN) test. The Nearest Neighbor test uses two parameters, R and c. R is the ratio between the mean NN distance $\overline{r_a}$ and the expected mean NN distance $\overline{r_e}$, and c is a parameter that evaluates the significance of R (Clark and Evans, 1954). R and c are calculated as follows:

$$R = \frac{\overline{r_a}}{\overline{r_e}} \tag{2.3}$$

$$c = \frac{\overline{r_a} - \overline{r_e}}{\sigma_e} \tag{2.4}$$

where σ_e is the expected standard deviation. The method by Clark and Evans (1954) uses a Poisson distribution. According to Hamilton et al. (2013), the angular distances between pairs of points of a uniform random distribution, as used in Equations 2.1 and 2.2, approximates that of a Poisson distribution. Thus, using this Poisson distribution, $\overline{r_e}$ and σ_e are calculated as follows for a sample size N and area A:

$$\overline{r_e} = \frac{1}{2\sqrt{N/A}} \tag{2.5}$$

$$\sigma_e = \frac{0.26136}{\sqrt{N^2/A}} \tag{2.6}$$

A value of $R = 1$ and $c = 0$ implies that the tested distribution is randomly distributed. The 1, 2, and 3σ confidence intervals are calculated for R and c as a function of the number of points. This is illustrated in Figure 2.5. If the value for R is below its -3σ confidence interval, the distribution can be considered clustered relative to a random distribution. If the value for R is above its $+3\sigma$ confidence interval, the distribution can be considered more spatially uniform than expected for a random distribution (Hamilton et al., 2013). The value for c is used to determine if the value for R is statistically significant. If both R and c are outside their respective 3σ confidence intervals, then the tested distribution exhibits a significant departure from a random distribution. If R and c are both within the 3σ confidence interval, there is no significant departure from randomness. Finally, the results can be considered inconclusive if R is outside its 3σ confidence interval but c is not, or vice versa (Hamilton et al., 2013).

Applying the Nearest Neighbor test on Io's volcanic distribution, as discussed in the previous section, results in a value of $R = 0.7987$ and -10.8490. As illustrated in Figure 2.5, the values for R and c are far below their respective -3σ confidence intervals. Since both the R and c are below their -3σ confidence intervals, Io's distribution exhibits a statistically significant departure from randomness and towards clustering.

After determining the Nearest Neighbor parameters, random clusters can be generated that match these parameters. This is done by combining the random distribution from the previous section with random noise. The process of generating a clustered random distribution with N data points is split up into several steps.

First, noise is generated in a 180° by 360° grid with a value between 0 and 1. In the case of this thesis, Fractional Brownian Motion (FBM) (Mandelbrot and Van Ness, 1968) is used due to its low processing time. An example of Fractional Brownian Motion is illustrated in Figure 2.6a. After the

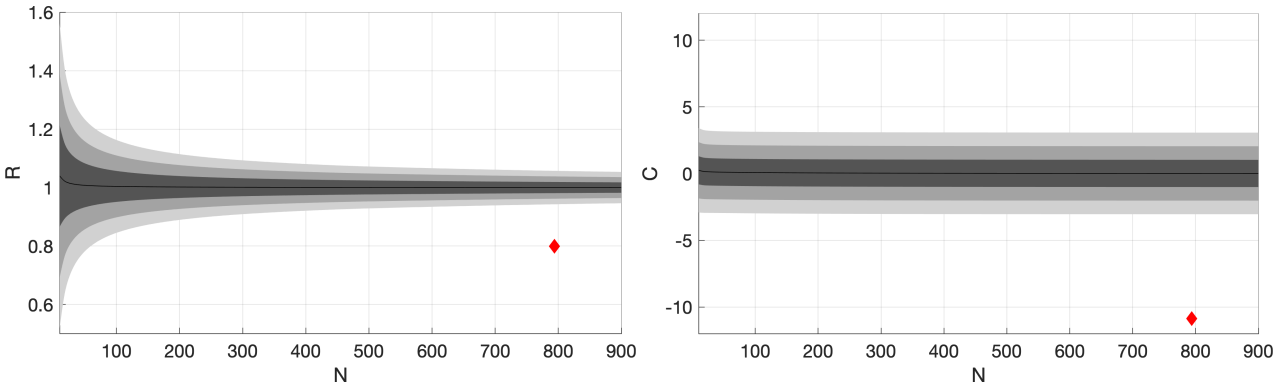

(a) (b)

Figure 2.5: Nearest Neighbor results for Io's volcanic distribution. Y-axis represents the values for R (a) and c (b), x-axis represents the number of data points analyzed. Shaded areas indicate the 1, 2, and 3 sigma confidence intervals. Red diamond indicates the values for Io's volcanic distribution. Images generated using the Geologic Image Analysis Software by Beggan and Hamilton (2010).

noise is generated a random number between $0.1N$ and $0.6N$ successive (in magnitude) points are extracted from the noise grid and saved as coordinates. A number between $0.1N$ and $0.6N$ is used to speed up the iterative process. From performed tests, no samples fit the required parameters when more than $0.6N$ noise points were used and samples with less than $0.1N$ noise points had significantly larger error than samples with more than $0.1N$ noise points. The extracted points can be seen in Figure 2.6b.

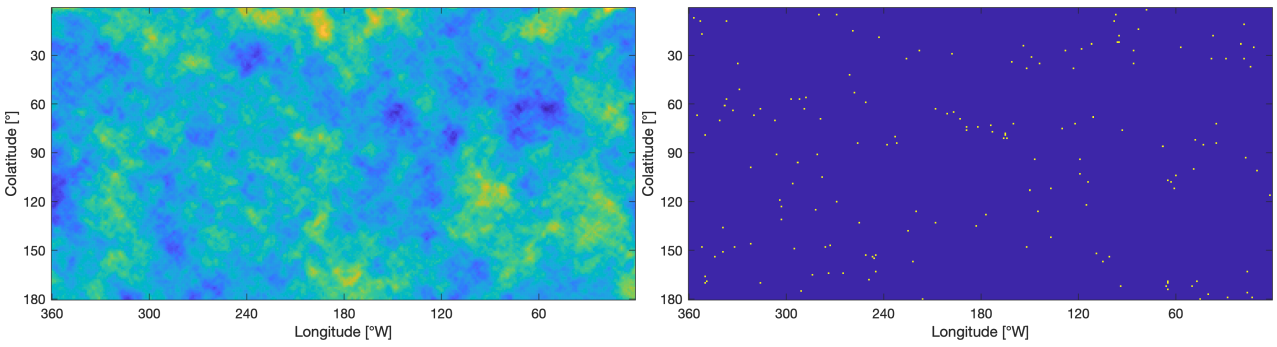

(a) (b)

Figure 2.6: The noise grid generated using Fractional Brownian Motion (a) and the extracted noise points (b).

Second, the saved noise points are supplemented with random data points, generated using Equation 2.1 and Equation 2.2, until the sample data set has the required N data points. This step is done to ensure that the generated distribution has a similar spatial distribution to that of Io, i.e. fairly evenly spaced longitudinally and weighted towards the equator latitudinally. The spatial distribution of Io's volcanic centers are illustrated in illustrated in Figure 2.4. If only the points extracted from the Fractional Brownian Motion are used, the R and c value could still match that of Io. However, it could not match its spatial distribution. Therefore, the saved noise points have to be supplemented with random data points.

Next, several tests are performed on the N data points to ensure the distribution matches the clustering of Io's volcanic distribution. First, a simple check is performed to determine if the majority of data points are located at lower latitudes as opposed to higher latitudes. This check is performed by counting the number of data points in 5 bins between 0 and 180 degrees colatitude with a size of 36 degrees each. As it is expected that the majority of the data points are located near the equator, the third bin, between 72 and 108 degrees, should be the largest. The second and fourth bins, between 36 and 72 and between 108 and 144, should then contain fewer points

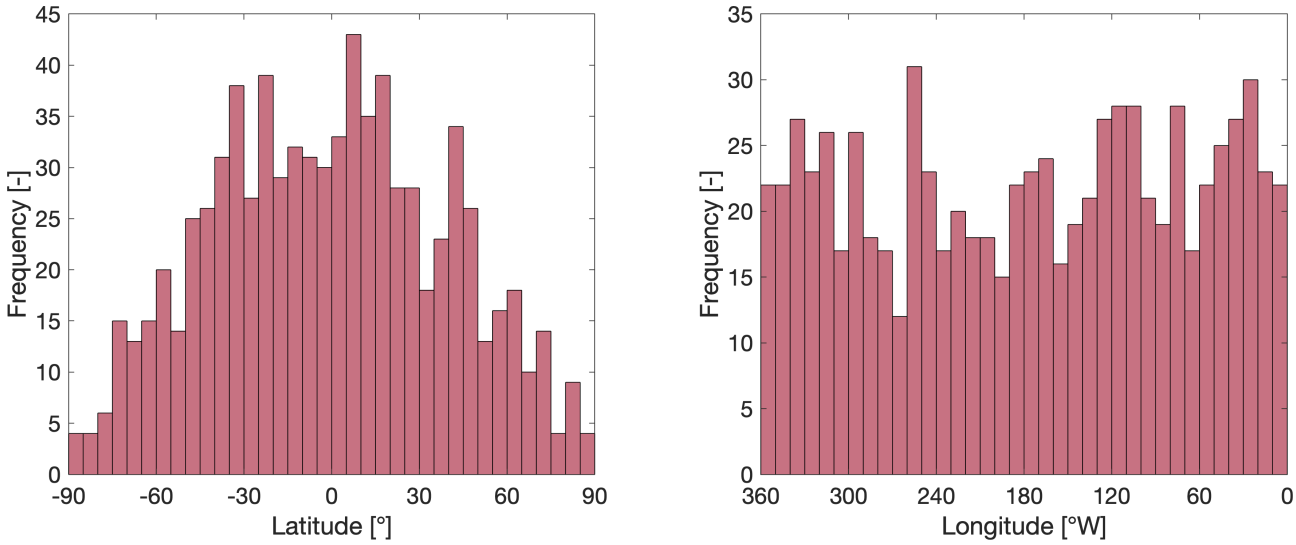

Figure 2.7: A pair of histograms of the spatial distribution of the latitude (left) and longitude (right) of a sample clustered random distribution containing 794 points. The bin size is equal to 5° (left) and 10° (right).

than the third bin but more points than the first and fifth bins. As previously mentioned, this is to take the decrease in surface area at higher latitudes into account. There could still be a slight bias towards the poles. However, this should not significantly influence the final results. If the generated data set passes this test, the next test is performed. If it fails, a new data set is generated. The second test determines the Nearest Neighbor R and c parameters of the generated data set. If the values of R and c are both within 10% of the values of Io's volcanic distribution, the generated data set is kept.

This process is repeated until the required number of sample data sets are generated. Figure 2.7 illustrates a histogram of a sample clustered random distribution generated, with similar R and c values as Io's volcanic distribution, using the aforementioned method.

The algorithm described in this section is not yet perfect. The current algorithm does not simulate the underlying mechanisms that could result in the clustering of volcanic centers but mimics the surface pattern that could occur. Thus, there may be unexplored biases in the generation of these volcanic clusters. Such as, how the resolution of the noise grid influences the generated distribution or if the implementation of Fractional Brownian Motion has unknown biases. However, it does function well enough to aid in investigating this thesis' hypothesis.

2.3. Spherical Harmonic Analysis

This section will use a spherical harmonic analysis to quantitatively examine the spatial distribution of Io's volcanic centers on a global scale. Spherical harmonics allow for the analysis of a distribution on a sphere, it shows where volcanic centers are concentrated and at which wavelength. This is done through the use of harmonic coefficients. These coefficients allow for determining the spatial density of volcanoes and if Io's volcanic distribution deviates from randomness at a certain spherical harmonic degree l (Ribe and De Valpine, 1994).

2.3.1. Methodology

The equations used in this analysis are similar to the equations used by Kirchoff et al. (2011). This method is chosen as it allows for the input of a discrete number of data points, as opposed to using a grid or field. For the purpose of this thesis, all data points are weighted equally. The equation for the spherical harmonic coefficients of degree m and order l is (Kirchoff et al., 2011; Johnson and

Richards, 2003):

$$\left.\begin{matrix} C_{lm} \\ S_{lm} \end{matrix}\right\} = \frac{(-1)^m}{4\pi}\sqrt{\frac{(2-\delta_{0m})(2l+1)(l-m)!}{(l+m)!}}\sum_{n=1}^{N} P_l^m(\cos\theta_n)\begin{cases}\cos m\phi_n \\ \sin m\phi_n\end{cases} \tag{2.7}$$

where N is the total number of volcanic centers in the distribution, δ is the Kronecker delta function, P_l^m is the associated Legendre polynomial, θ_n is the colatitude, ϕ_n is the longitude.

This specific normalization is chosen so that C_{00} is equal to the average number of data points per unit area of a unit sphere, $C_{00} = N/4\pi$. The spherical harmonic coefficients can then be used to reconstruct the field $f(\theta,\lambda)$ using the following expression (Kirchoff et al., 2011; Sneeuw, 1994):

$$f(\theta,\lambda) = \sum_{l=0}^{\infty}\sum_{m=0}^{l}\frac{(-1)^m}{R^2}\sqrt{\frac{(2-\delta_{0m})(2l+1)(l-m)!}{(l+m)!}}P_l^m(\cos\theta)\left(C_{lm}\cos m\phi + S_{lm}\sin m\phi\right) \tag{2.8}$$

where R is the radius of Io, equal to 1821.6 km (Schubert et al., 2004). The factor $1/R^2$ is added to normalize the field to volcanic centers per unit area. As seen in this equation, the field is only truly reconstructed when degree $l = \infty$ is reached. However, the goal of spherical harmonics is not to fully reconstruct the field but to create a smoothed version by truncating at a desirable degree l yielding only the required specificity.

To test the statistical significance of the spherical harmonic coefficients at different degrees, the spectral power and the standard deviation are calculated. The spectral power provides information about which degree, and its equivalent wavelength, contains the most signal of the analyzed distribution (Kirchoff et al., 2011). The spectral power at degree l, S_l^2, and the standard deviation, σ, can be determined as follows (Kirchoff et al., 2011; Ribe and De Valpine, 1994):

$$S_l^2 = \frac{(4\pi)^2}{N(2l+1)}\sum_{m=0}^{l}\left(C_{lm}^2 + S_{lm}^2\right) \tag{2.9}$$

$$\sigma = \sqrt{\frac{2(N-1)}{N(2l+1)}} \tag{2.10}$$

A normalization factor of $(4\pi)^2/N(2l+1)$ is applied to the equations in order to ensure that a random distribution of objects on a sphere will appear flat or "white" (Kirchoff et al., 2011; Richards et al., 1988). For a random distribution, this results in a mean of 1 for all degrees l and a standard deviation equal to σ as described in Equation 2.10.

A value for the spectral power at degree l significantly different from unity indicates a significant density variation for the respective wavelength. This would indicate a physical mechanism behind the specific distribution. To test for deviation from unity, the spectral power is plotted against 1, 2, and 3σ confidence intervals for each degree, with the standard deviation as calculated with Equation 2.10. A value for the spectral power significantly above 3σ can be considered a significant deviation from randomness.

2.3.2. RESULTS

Using the filtered volcanic distribution, as mentioned in Section 2.1, the spherical harmonic analysis was performed. The expansion was truncated at degree 30. This degree results in an equivalent wavelength of $2\pi r/l = 382$ km. This is well within the order of the distance between neighboring volcanic centers, as the largest distance between neighboring volcanic centers is approximately 400 km. As the method described in the previous section is a discrete process, the truncation does not affect the calculated spherical harmonic coefficients or spectral power (Kirchoff et al., 2011).

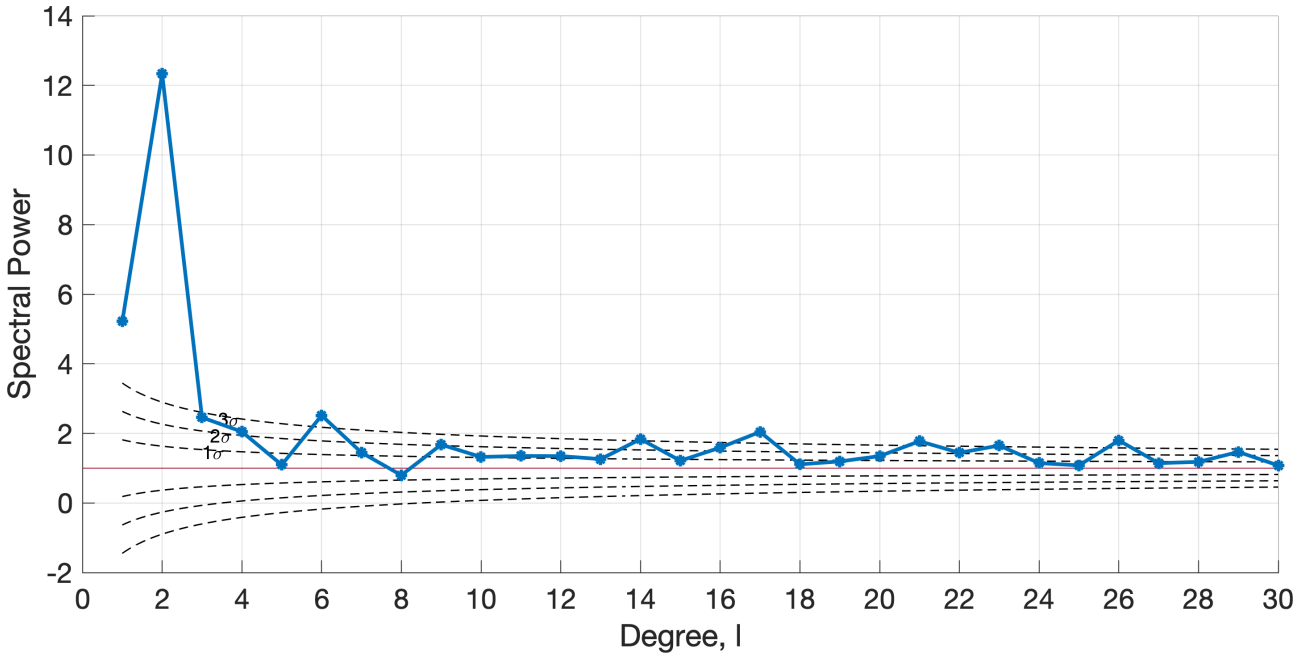

Figure 2.8: The normalized spectral power for the distribution of Io's volcanic centers, truncated at $l = 30$, in blue. The black dashed lines indicate the 1, 2, and 3 sigma confidence interval for a random distribution.

The spectral power is calculated up to degree $l = 30$ and is illustrated in Figure 2.8. This figure shows that a statistically significant peak, far over the 3σ range, is present at degree $l = 2$. A secondary peak is present at degree $l = 1$, and minor peaks, just above the 3σ level, are found at $l = 6, 14, 17, 21$, 23, and 26. The significance of signals at higher degrees likely indicate different physical phenomenon than at lower degrees. The lower degrees likely indicate large-scale effects, while higher degrees indicate smaller, more localized, effects.

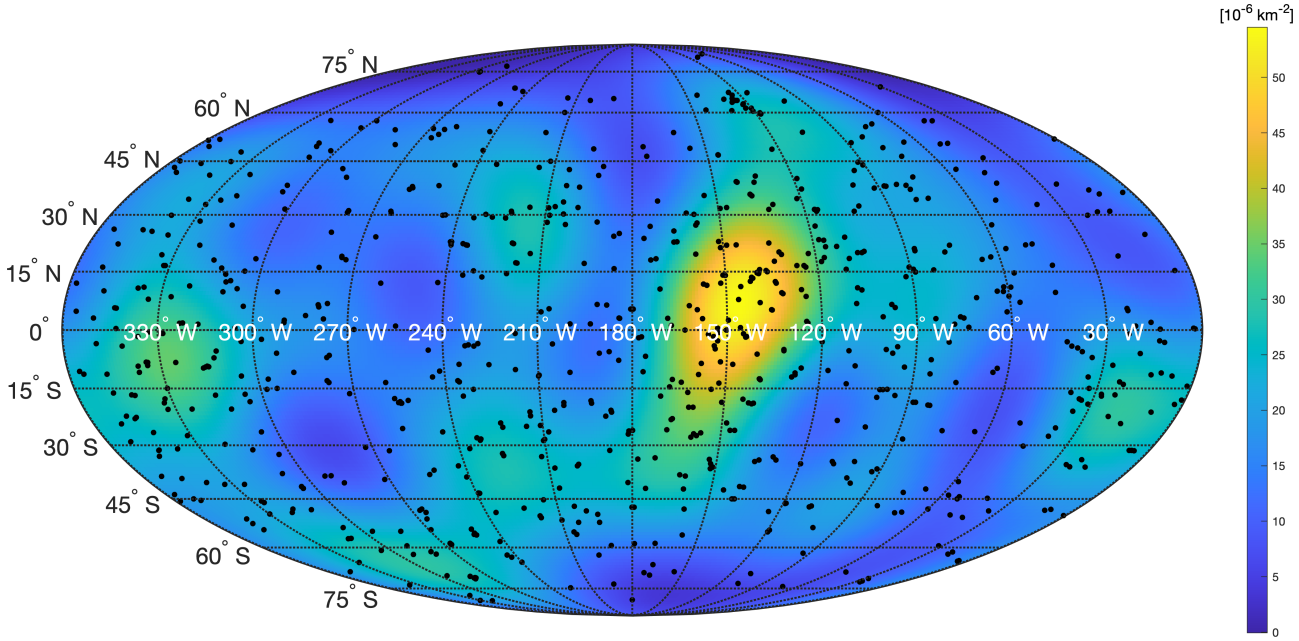

Figure 2.9: Mollweid projection of the spherical harmonic representation of Io's volcanic distribution truncated at degree $l = 6$. Black dots represent volcanic centers. Average volcanic center density is 19 per 10^6 km^2. Color bar ranges from -0.04 to 54.5 per 10^6 km^2. The negative values are due to spectral truncation (Kirchoff et al., 2011).

Figure 2.9 shows a pseudocolor plot of the spherical harmonic field, truncated at degree $l = 6$. The expansion is truncated at this degree, in order to better illustrate the more statistically signif-

icant degrees. The strong degree $l = 2$ signal indicates a large number of volcanic centers near the equator. The peak at degree $l = 2$ is consistent with the asthenospheric heating model (Segatz et al., 1988). However, the degree $l = 1$ signal indicates more volcanic centers towards the antijovian hemisphere of Io. This does not match any tidal heating model, as these are quite symmetric (Segatz et al., 1988; Hamilton et al., 2013; Tyler et al., 2015). The asymmetry towards the antijovian hemisphere verifies the longitudinal distribution seen in Figure 2.4. Although, as previously noted, this may be a slight observational bias due to the higher resolution data available of this region.

Figure 2.9 shows two concentrations of volcanic centers located around the equator near 330°W and 150°W. The location of these concentrations can mainly be attributed to the significant degree $l = 2$ signal and indicates a 30° offset with respect to the tidal axis and predicted surface heat flux maxima, similar to the offset found by Hamilton et al. (2013) and de Kleer and de Pater (2016). While the strong degree $l = 2$ signal is consistent with the asthenospheric heating model, no significant degree $l = 4$ is present. The peak at $l = 6$ indicates that several smaller scale concentrations of volcanic centers are spread around Io. This peak is similar to that found by Kirchoff et al. (2011).

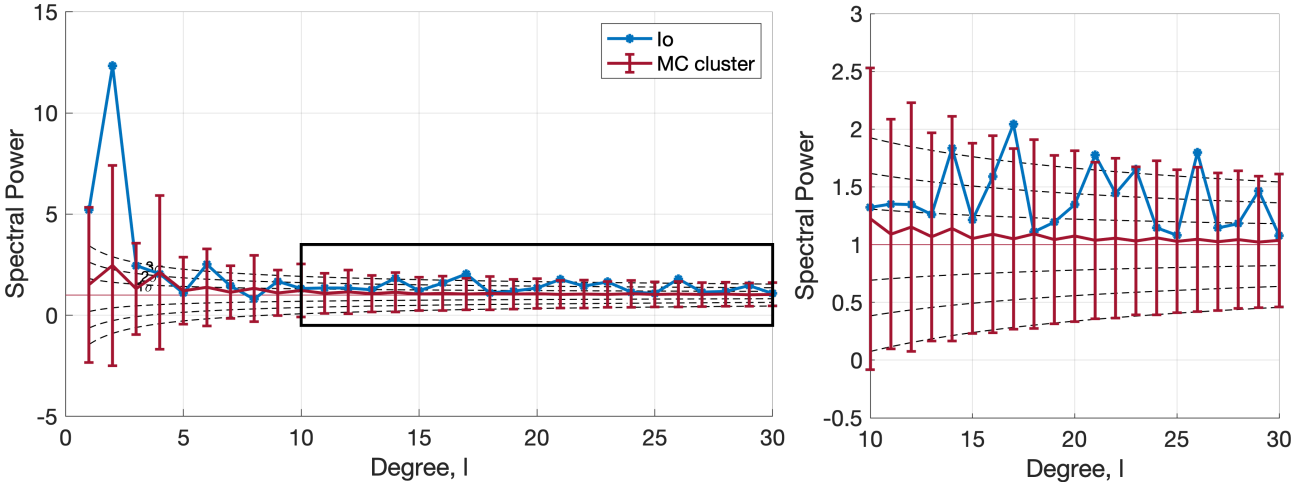

Figure 2.10: Monte Carlo analysis of the spectral power of 1000 clustered random distributions (red) compared to the spectral power results for Io's volcanic distribution (blue). Dotted black lines illustrate a 3-sigma confidence interval for a random distribution. The red error bars show a 3-sigma confidence interval for the Monte Carlo analysis. Negative values seen in the error bars are caused by the 3-sigma confidence interval around the mean values (red line). Individual results cannot become negative (Equation 2.9).

For higher harmonic degrees, the spectral power contains more energy compared with a random distribution. This may indicate clusters at these degrees. To test if the peaks in the spectral power are due to clustering, a Monte Carlo Analysis is performed. This Monte Carlo Analysis will use 10,000 sample data sets containing 794 clustered random data points. These data sets are generated as discussed in Section 2.2. For each data set, the spherical harmonic coefficients and spectral power are calculated. The mean and standard deviation of the spectral power for each degree for the Monte Carlo analysis is determined and used to determine the deviation of the Io's spectral power with respect to the simulated mean.

The spectral power of the Monte Carlo analysis for a clustered random distribution is depicted in Figure 2.10. As seen in this figure, the statistically significant peaks at degrees $l = 1$ and 6 for Io's distribution can be explained by the random clustering of the volcanic centers. The same cannot be said for the strong peak at degree $l = 2$. Although the peak can be partially explained by random clustering, there is another physical process causing the significant density variation at this degree. This is further investigated by comparing the spherical harmonics to the diurnal stresses on Io in Chapter 4. Similarly, much of statistical significance at higher degrees, especially degrees $l = 14, 23$, can potentially be explained due to clustering.

2.4. CURVE RECONSTRUCTION

This section will use a curve reconstruction algorithm to find connections and patterns between volcanic centers on a more local scale. A curve reconstruction algorithm reconstructs curves and shapes from a set of unorganized points. This method will allow for determining potential chains of volcanic centers, the connections between them, and what directions the chains are facing. Potential chains of volcanoes could indicate that volcanic eruptions are linked to crustal faults or propagated through stress-induced fractures in the lithosphere.

2.4.1. METHODOLOGY

As curve reconstruction algorithms have not yet been applied to planetary bodies, a special algorithm is developed for this purpose using MATLAB. This algorithm is based on the two-dimensional (2D) Conservative-Crust algorithm by Dey et al. (2000). The Conservative-Crust algorithm is adapted to three-dimensional geometry to account for the curvature of the surface and the fact that, for example, a volcanic center at 1°W might be connected to a volcanic center at 359°W. The algorithm depends on two inputs, a set of points on a sphere P and a non-negative real parameter ρ. These inputs are used to construct a graph G, which is a collection of open and closed chains with vertices in P.

The algorithm is structured as follows:

1. Compute the Delaunay triangulation $\mathcal{D}(P)$
2. Extract the Gabriel graph $\mathcal{G}(P) \subseteq \mathcal{D}(P)$
3. Compute the graph $G \subseteq \mathcal{G}(P)$, where $e \in \mathcal{G}(P)$ is in G' if and only if $B(e, l(e)/\rho)$ is a V-ball.

The structure of the algorithm is the same as that of the two-dimensional Conservative-Crust algorithm. The adaptation for three-dimensions is in the execution of these steps.

First, the Delaunay triangulation $\mathcal{D}(P)$ is computed using the built-in MATLAB function. A Delaunay triangulation is a set of interconnected triangles with vertices in P defined so that there are no points of P within any of the triangles. This is illustrated in Figure 2.11a). To determine the edges e of the Delaunay triangulation that connects along the surface of the sphere, a convex hull is extracted.

Second, the Gabriel graph $\mathcal{G}(P) \subseteq \mathcal{D}(P)$ is extracted. The Gabriel graph consists only of vertices with Gabriel edges. A Delaunay edge is also a Gabriel edge if there are no other points in P within a radius of half an edge length, $l(e)/2$, of the midpoint of the edge.

Finally, the graph G is computed. This step uses the parameter ρ to determine if a ball around edge e is a Voronoi ball or V-ball. This ball is written as $B(e, l(e)/\rho)$, with e indicting the midpoint of edge e and $l(e)/\rho$ the radius of the ball, the length of the edge divided by the parameter ρ.

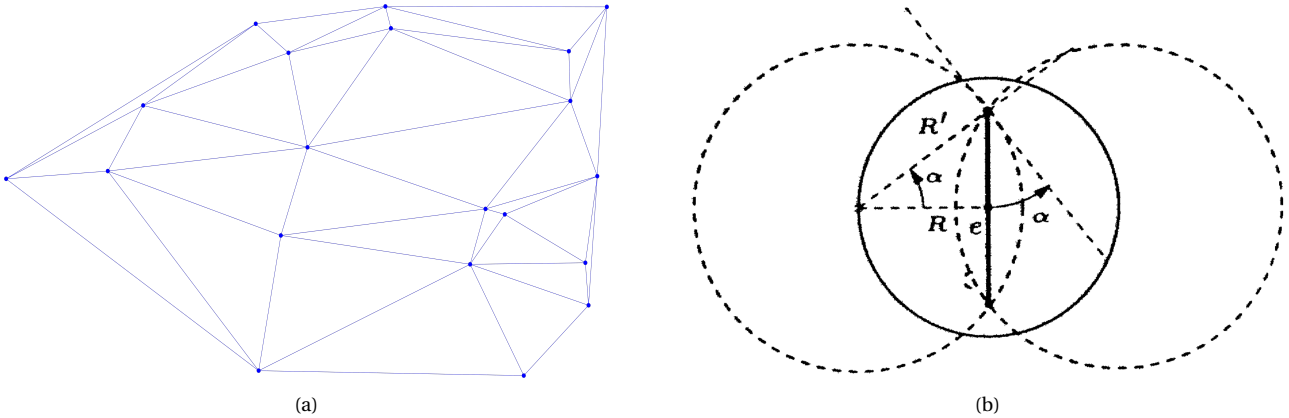

(a) (b)

Figure 2.11: (a) An example of Delaunay Triangulation for a random points set P. As can be seen, there are no points of P within any of the triangles. (b) An illustration of the V-ball (solid circle) of edge e, with its implied D-ball (dotted circle), projected on a two-dimensional surface. Image obtained from Dey et al. (2000).

A ball $B(e,R)$ is a V-ball if its edge e has two Delaunay balls or D-balls of radius $R' = \sqrt{R^2 + (l(e)/2)^2}$ (Dey et al., 2000). With a D-ball being defined as a ball that is empty of points P. This is illustrated in Figure 2.11b. If the Gabriel edge e is a V-ball then that edge is a part of graph G. This process is repeated for each edge in the Gabriel graph.

To test the performance of the curve reconstruction algorithm on a spherical body, two circles are plotted on the equator of a sphere. Circles are used to verify the performance of the algorithm as they are a relatively simple shape and have been used in the verification of other curve reconstruction algorithms in Dey et al. (2000). Random noise points are added to test if the algorithm can still reconstruct the circles, this is illustrated in Figure 2.12. As can be seen in this figure, the algorithm holds up well with random noise added. Although each circle only consists of 31 data points, the shapes are still clearly definable when 100 and 200 noise points are added.

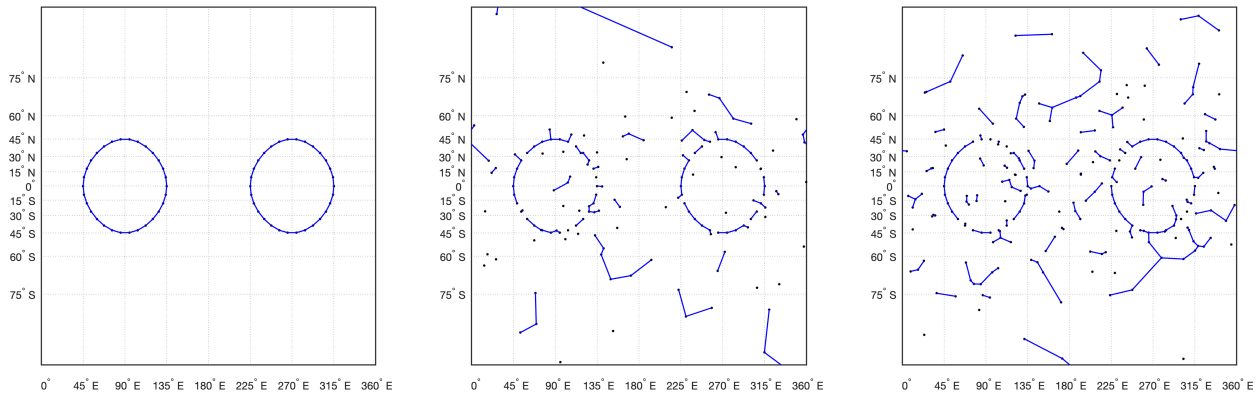

(a) (b) (c)

Figure 2.12: Mercator projection of four circles on a sphere with (a) no noise points added (b) 100 noise points added (c) 200 noise points added.

Figure 2.13 illustrates the effect of parameter ρ on the curve reconstruction algorithm. As can be seen in this figure, a lower value for ρ (Figure 2.13b) does not fully reconstruct the shapes. In contrast, a higher value for ρ (Figure 2.13d) clearly shows the shape, however, the elements start connecting. A value of ρ that is too low may not form the connections in data points, while a value of ρ that is too high may over-connect and form too many connections. This illustrates the algorithms reliance on the parameter ρ and the existence of an optimal value of ρ.

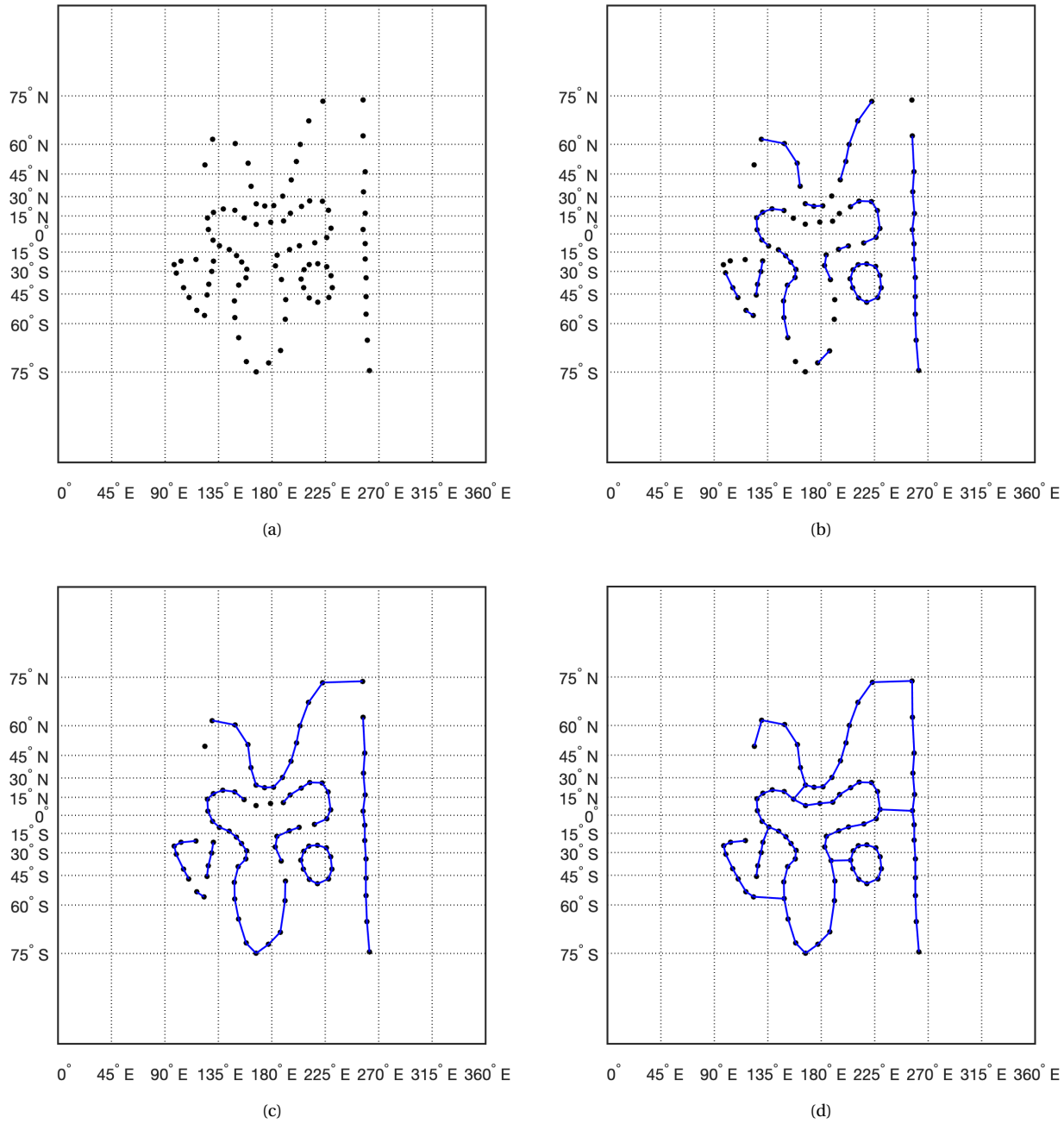

Figure 2.13: The effect of parameter ρ using a Mercator projection of shapes defined by Dey et al. (2000) projected on a sphere with (a) $\rho = 0.0$ (b) $\rho = 1.25$ (c) $\rho = 1.75$, and (d) $\rho = 4.0$.

2.4.2. RESULTS

This section describes analysis of Io's volcanic distribution, as described in Section 2.1, using the curve reconstruction algorithm.

First, an optimal value of the parameter ρ is selected. This is achieved by comparing the number of larger chains, those with three or more volcanic centers in a chain, with the average length of these chains. This selection process is a trade-off. Choosing a larger value for ρ results in more and longer chains being generated but it does not exclude any of the potentially smaller chains. However, choosing a value of ρ that is too small will exclude larger chains. Thus, a balance has to be found between knowing a large number of volcanic chains and their locations, while still being confident in that they represent actual volcanic chains

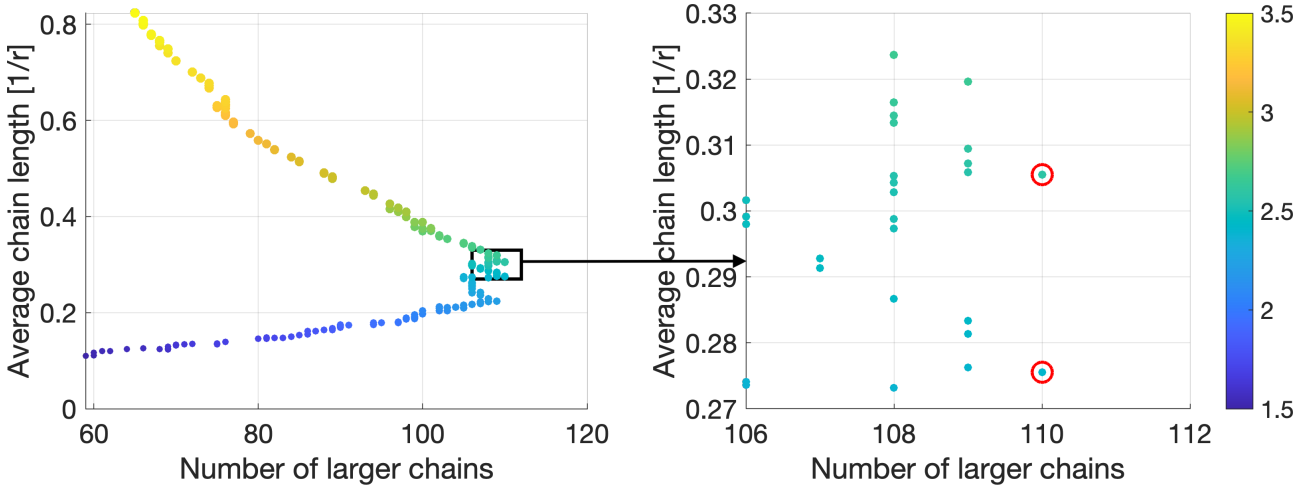

Figure 2.14: The average chain length as a function of the number of larger chains. Each dot represents a value of ρ between $\rho = 1.5$ and $\rho = 3.5$ with steps of 0.01. The average chain length is in fractions of Io's radius. The red circles indicate the two identified optimal values for ρ.

The comparison is performed for values of ρ between $\rho = 1.5$ and $\rho = 3.5$. A step size of 0.01 is used, as smaller step sizes will not have a significant impact on the results. The average chain length as a function of the number of larger chains is illustrated in Figure 2.14. As can be seen in this figure, two possible optimal values for ρ are determined: $\rho = 2.41$ and $\rho = 2.59$. Both values of ρ generate 110 larger chains at an average length of 0.276 Io radii and 0.306 Io radii, respectively.

As ρ has no physical basis, a comparison is made with Earth to determine which value is to be used. This is done by determining the average length of long volcanic chains on Earth. A list of long linear volcanic chains is obtained from Table 7 of Jackson (1976), the chains in this list all formed due to hot spot volcanism, as opposed to plate tectonics, this matches the proposed mechanism of volcanism on Io. Using this list, the average length was calculated to be 1542 km or ≈ 0.242 Earth radii. Therefore, a value of $\rho = 2.41$ is selected.

Figure 2.15 shows the reconstructed curves at $\rho = 2.41$. As can be seen in this figure, there are numerous shorter chains and a handful of longer chains. The shorter chains dominate the antijovian hemisphere, centered around 180°W, while the larger chains dominate the subjovian hemisphere, centered around 0/360°W. Unlike chains of volcanoes on Earth, illustrated in Section A.1, there is no apparent pattern in the direction of the chains on Io. This is also reflected in different values of ρ obtained for Earth and Io. For a more complete list of 650 volcanoes on Earth, obtained from Sigurdsson et al. (2015), a value of $\rho = 3.2$ is found to be optimal. The ρ is significantly larger as volcanism on Earth is dominated by subduction and mid-ocean ridges (Sigurdsson et al., 2015), resulting in long chains of volcanoes.

To investigate the significance of the generated curve reconstruction two Monte Carlo analyses

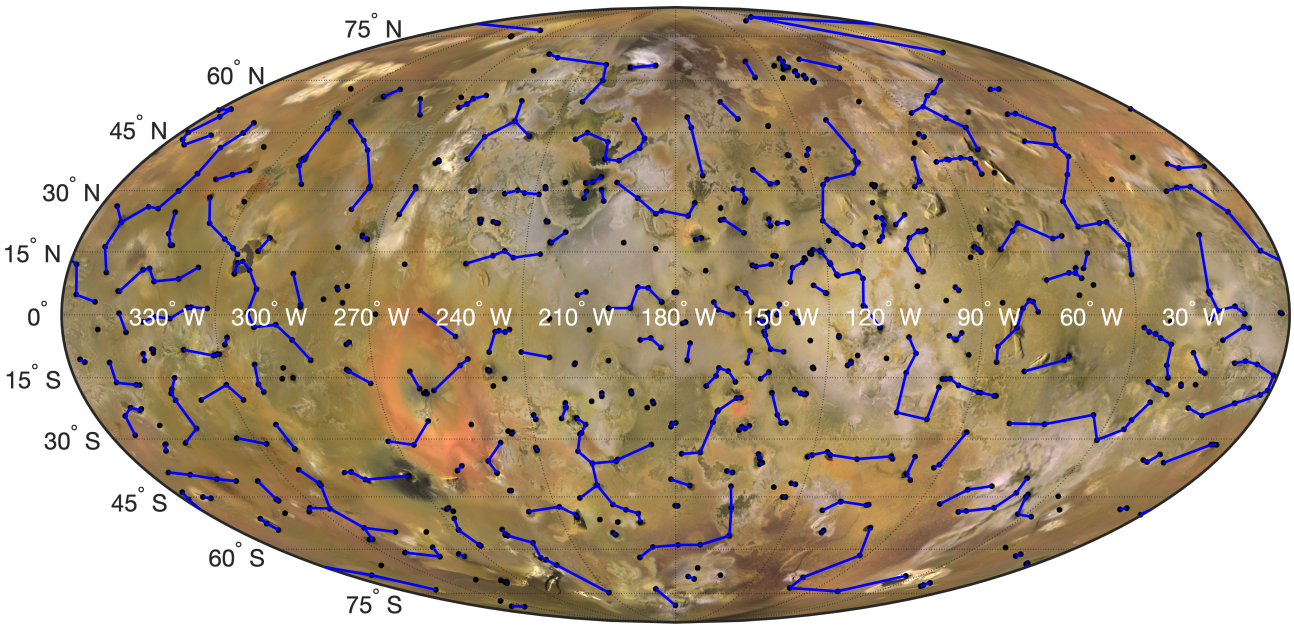

Figure 2.15: Mollweide projection of the reconstructed curve for 794 volcanic centers at $\rho = 2.41$.

are performed. First, a simulation of 10,000 data sets, containing 794 data points with a random distribution, are generated. Second, a simulation of 10,000 data sets, containing 794 data points with a clustered random distribution, are generated. For each sample, a curve reconstruction is performed, at $\rho = 2.41$, and several parameters are examined. This allows for determining the deviation of these parameters for Io from the simulated mean.

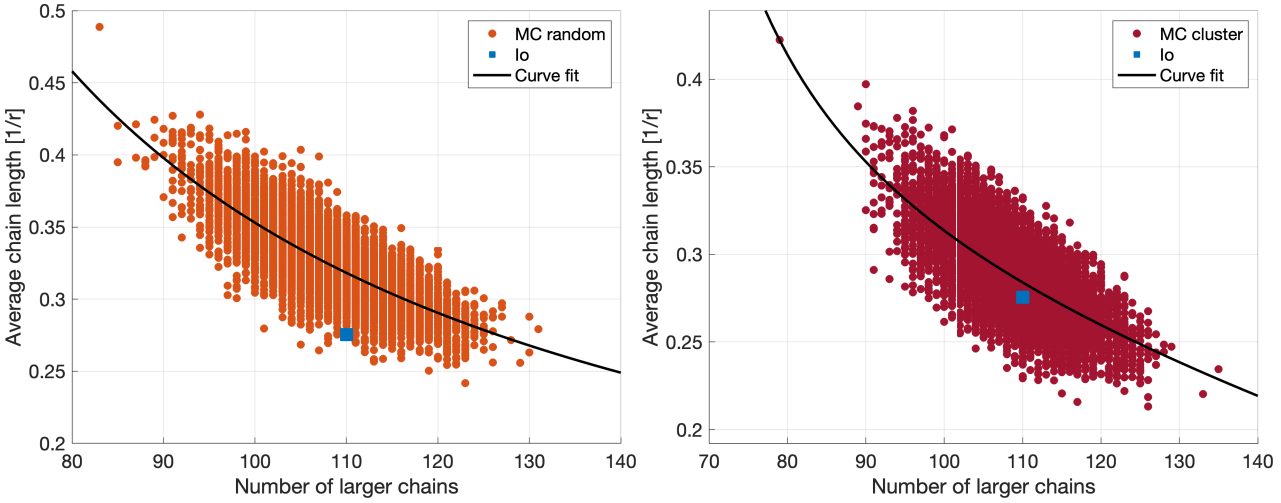

Figure 2.16: The average chain length of larger chains as a function of the number of larger chains for (a) a random distribution and (b) a clustered random distribution. Black line indicates an rational curve fit through the Monte Carlo analysis results.

First, the number of larger chains and the average length of these chains, similar to the parameters used to select the value of ρ, are examined. This analysis is performed to examine if the number of larger chains and their average length exhibit unusual behavior. For example, if Io were to have fewer larger chains but with a larger average length than expected for a random or clustered random distribution, this would indicate that the average chain is longer than expected and contains more volcanic centers. The average length of larger chains as a function of the number of larger chains of both random and clustered random distributions are plotted in Figure 2.16. Figure 2.16a

shows that the number of larger chains and their average length for Io's distribution is just within two standard deviations from the mean of the Monte Carlo simulation. This shows that the average length of the longer chains is on the low end for the number of longer chains given the value of ρ used in the simulation, although it is not statistically significant. Figure 2.16b shows that the number of larger chains and their average length for Io's distribution is well within the expected range for a slightly clustered volcanic distribution.

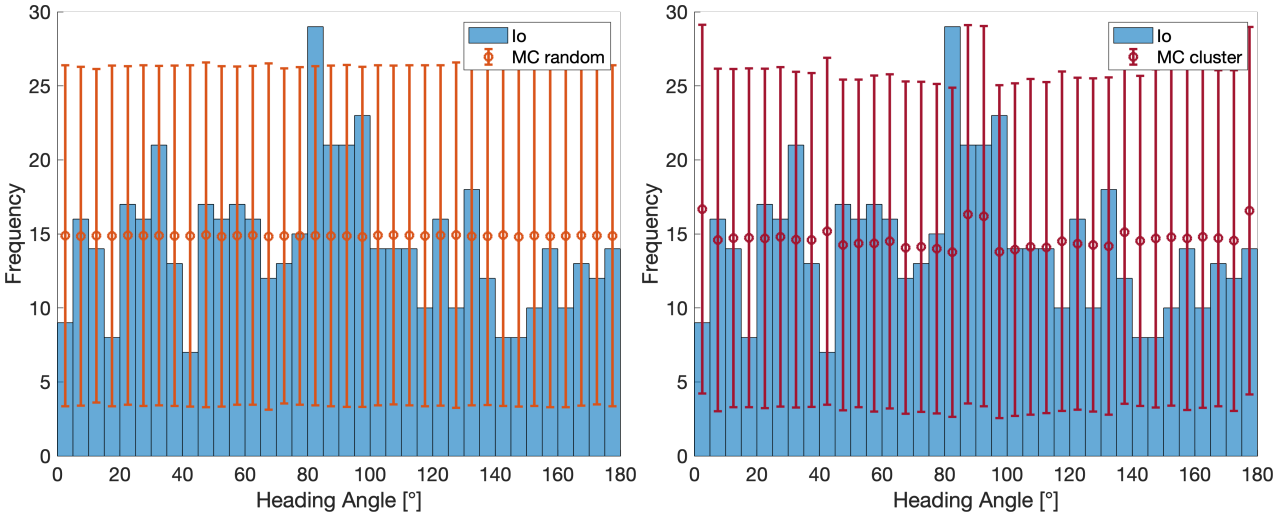

(a) (b)

Figure 2.17: Histogram of the heading angle of the curve reconstruction of Io's volcanic distribution. Error bars represent a 3-sigma confidence interval of the histogram of the heading angle for the Monte Carlo analysis of (a) a random distribution and (b) a clustered random distribution.

Second, the angle each individual edge makes with respect to the north pole, referred to as the heading angle, is analyzed. Histograms of the heading angle, overlain with a 3σ confidence interval of the heading for the two Monte Carlo analyses, are illustrated in Figure 2.17. The figures show that, with the exception of a peak between 80 and 85 degrees, the heading angle of Io's curve reconstruction are all within the 3-sigma confidence interval for both the random and clustered random distributions. The 3-sigma confidence interval for the clustered random distribution appears to have peaks around 0, 180, and 90 degrees. This is likely an artifact of the cluster generating algorithm, indicating that the algorithm is not yet perfect. However, it does not significantly influence the results. The peak at 80-85 degrees motivates further investigation into the orientation of the edges. This is done by comparing the reconstructed curves on Io to the direction of the tensile diurnal stresses on Io in Chapter 4.

3
SURFACE STRESS ANALYSIS

As Io orbits around Jupiter, the forces it experiences change slightly due to tides caused by its eccentricity. These eccentricity-driven, also referred to as diurnal, tidal forces result in friction within Io and result in significant stresses on Io. These tidally induced stresses are dissipated and in the case of Io result in significant volcanism (Peale et al., 1979). The stresses can also be relieved through failure of the lithosphere, similar to the cracks in Europa's ice (Greenberg and Geissler, 2002). To determine if the stresses also play a role in the location of Io's volcanic centers, the diurnal stresses are analyzed. It is assumed that the potential failures of the lithosphere are related to the diurnal stresses, as opposed to other phenomena.

First, Io's interior is analyzed. This allows for the determining of Io's tidal response due to diurnal forces. Following this, the elastic and viscoelastic diurnal stresses are described. Finally, the diurnal stresses are used to determine the stresses along Io's principal axis at the surface. In the next chapter, the direction and magnitude of the principal stress are compared to the significant density variations found in the volcanic distribution and significant orientation of the volcanic chains found in the previous section.

3.1. INTERIOR OF IO

To determine the response of Io's interior due to the time-dependent tidal forces, the interior is modeled using several layers. These layers are assumed to be uniform Maxwell-viscoelastic spherical layers. For each of the layers, the thickness, rigidity, density, and viscosity are used to describe the layer. The model of Io's interior is then used to perform a normal modes analysis to determine the tidal Love numbers (Jara Orué, 2016).

Table 3.1: Values for the structural parameters of the four layers considered in the modeling of Io's interior. Based on the asthenospheric heating model from Segatz et al. (1988).

Layer	Outer Radius R [km]	Density ρ [kg/m^3]	Shear Modulus μ [Pa]	Viscosity η [Pa·s]
Lithosphere	1821.6	3200	$65 \cdot 10^9$	10^{23}
Asthenosphere	1791.6	3200	$4.0 \cdot 10^4$	10^{10}
Mantle	1741.6	3200	$60 \cdot 10^9$	10^{21}
Fluid Core	980	5150	0	0

As previously mentioned, two end-member tidal heating models have been developed for Io, the asthenospheric heating model, and the deep mantle heating model (Segatz et al., 1988). Both models have a fluid core, a viscoelastic mantle, and a thin almost elastic lithosphere. In addition to these layers, the asthenospheric heating model has a viscoelastic low-viscosity asthenosphere between the lithosphere and mantle. The strong degree $l = 2$ pattern from the spherical harmonic analysis in Section 2.3 fits better with the dissipation pattern of the asthenospheric heating model.

Therefore, the four-layer model will be used. The structural parameters of the four layers need to fit the moment of inertia, the mean density, and the observed surface heat flow.

The lithosphere would need to be below 8 km thick to support Io's observed surface heat flow through conduction alone. This is incompatible with observed topography of up to 10 km (Gaskell et al., 1988). The hot spots and topography suggest convective heat transfer in the lithosphere (Segatz et al., 1988), therefore the thickness of the lithosphere is assumed to be 30 km, which is compatible with the topography. The lithosphere has a shear modulus of 60 GPa and a viscosity of 10^{21} Pa·s. To support the mean density and moment of inertia, Io is assumed to have a eutectic Fe-FeS core at a density of 5150 kg/m^3 (Segatz et al., 1988; Gaskell et al., 1988). As the core is assumed to be fluid, it will have a relatively low viscosity. Therefore, the core is assumed to be inviscid, i.e. have a viscosity of 0. Similarly, due to the core being fluid, it will have a shear modulus equal to zero. To match Io's significant tidal dissipation and relatively high mean density, the core is assumed to have a radius of 980 km (Segatz et al., 1988). The asthenosphere is assumed to be 50 km thick. To match the tidal dissipation and moment of inertia, the shear modulus and viscosity are assumed to be $4 \cdot 10^4$ Pa and 10^{10} Pa·s (Segatz et al., 1988). The densities of the lithosphere, asthenosphere, and mantle are all assumed to be 3200 kg/m^3. This in combination with the thicknesses of each layer match Io's mean density. The shear modulus and viscosity of the mantle are assumed to be slightly lower than the values for the lithosphere due to the higher temperatures (Segatz et al., 1988). The structural parameters for each of the layers are presented in Table 3.1.

The structural parameters are used to determine the tidal response of Io's interior due to tidal forces. Using the normal modes analysis program from Jara Orué (2016) the tidal response parameters are calculated. These parameters are presented in Table 3.2. The rows in this table represent the different relaxation modes. The first parameter, s_j, is the inverse relaxation time corresponding to the j-th relaxation mode. The radial Love numbers, h, are described in the third column. h_2^e represents the radial elastic Love number, while $h_{2,j}^v$ represents the radial modal Love number for the j-th relaxation mode. The tangential Love numbers, l, are described in the last column. Similar to the radial Love numbers, l_2^e represents the tangential elastic Love number, while $l_{2,j}^v$ represents the tangential modal Love number for the j-th relaxation mode. The fluid Love numbers for both l and h are calculated by summing up the values for elastic component and each j-th relaxation mode.

Table 3.2: Tidal response for the four layer model of Io's interior to diurnal tidal forces.

Mode	s_j [s^{-1}]	h_2^e or h_{2j}^v [-]	l_2^e or l_{2j}^v [-]
Elastic	-	$1.00108 \cdot 10^{0}$	$2.72979 \cdot 10^{-1}$
1	$-4.30840 \cdot 10^{-13}$	$7.68935 \cdot 10^{-1}$	$2.06336 \cdot 10^{-1}$
2	$-1.03700 \cdot 10^{-11}$	$3.39773 \cdot 10^{-2}$	$9.11746 \cdot 10^{-3}$
3	$-2.61780 \cdot 10^{-6}$	$4.74312 \cdot 10^{-1}$	$1.22927 \cdot 10^{-1}$
4	$-3.99970 \cdot 10^{-6}$	$3.58179 \cdot 10^{-7}$	$1.37339 \cdot 10^{-6}$

3.2. DIURNAL STRESSES

With the tidal Love numbers known, the diurnal stress field at Io's surface can be determined using the eccentricity-driven tidal potential. This section is split into three parts. First, the stresses induced by the elastic deformation are described. Second, the stresses induced by the viscoelastic deformation are described. Splitting up the stress components allows for clear insight into how much stress is generated by the deformations that induce them. Lastly, the two different components are calculated for the four-layer model of Io.

3.2.1. ELASTIC STRESSES

This section describes the equations used to calculate the elastically-induced stresses at the surface. As the stresses are calculated at the surface, the radial components of the stress tensor are equal to zero. This results in only three components that need to be evaluated (Jara Orué, 2016):

$$\begin{aligned}\sigma^{e}_{\theta\theta} = &\frac{1}{2}\frac{n^2 R\mu}{g_0}\frac{1}{\sqrt{1+\Lambda^2}}\Big\{-6e\beta^{\theta\theta}_{2,0}(\theta)\cos(nt+\angle\Lambda)\\ &+e\beta^{\theta\theta}_{2,2}(\theta)\left[4\sin(2\phi)\sin(nt+\angle\Lambda)+3\cos(2\phi)\cos(nt+\angle\Lambda)\right]\\ &+4\sin(\varepsilon)\beta^{\theta\theta}_{2,1}(\theta)\left[\cos(\phi)\sin(\varpi+nt+\angle\Lambda)\right]\Big\}\end{aligned} \tag{3.1}$$

$$\begin{aligned}\sigma^{e}_{\phi\phi} = &\frac{1}{2}\frac{n^2 R\mu}{g_0}\frac{1}{\sqrt{1+\Lambda^2}}\Big\{-6e\beta^{\phi\phi}_{2,0}(\theta)\cos(nt+\angle\Lambda)\\ &+e\beta^{\phi\phi}_{2,2}(\theta)\left[4\sin(2\phi)\sin(nt+\angle\Lambda)+3\cos(2\phi)\cos(nt+\angle\Lambda)\right]\\ &+4\sin(\varepsilon)\beta^{\phi\phi}_{2,1}(\theta)\left[\cos(\phi)\sin(\varpi+nt+\angle\Lambda)\right]\Big\}\end{aligned} \tag{3.2}$$

$$\begin{aligned}\sigma^{e}_{\theta\phi} = &\frac{1}{2}\frac{n^2 R\mu}{g_0}\frac{1}{\sqrt{1+\Lambda^2}}\\ &\times\Big\{2e\beta^{\theta\phi}_{2,2}(\theta)\left[4\cos(2\phi)\sin(nt+\angle\Lambda)-3\sin(2\phi)\cos(nt+\angle\Lambda)\right]\\ &+4\sin(\varepsilon)\beta^{\theta\phi}_{2,1}(\theta)\left[\sin(\phi)\sin(\varpi+nt+\angle\Lambda)\right]\Big\}\end{aligned} \tag{3.3}$$

where the Beta-functions are described in Equations 3.6 through 3.13, n is the mean motion [rad/s], R is the radius of Io [m], μ is the shear modulus [Pa], g_0 is the surface gravity [m/s^2], t is the time, ε is the obliquity, ϖ is the argument of periapsis, h and l are Love numbers as described in Table 3.2 and used in Equations 3.6 to 3.13, and Λ is the dimensionless ratio. The dimensionless ratio Λ and its angular variable $\angle\Lambda$ are defined as follows:

$$\Lambda = \frac{\mu/\eta}{n} \tag{3.4}$$

$$\angle\Lambda = \arctan(\Lambda) \tag{3.5}$$

According to Jara Orué (2016), the dimensionless ratio Λ can be described as the "relaxation state of diurnal stresses at the surface". This parameter will start to have a significant influence on the magnitude of the stress when it is approximately equal to 0.1. However, in the case of Io, with a shear modulus of $\mu = 65$ GPa and a viscosity $\eta = 10^{23}$ Pa·s, Λ is of the order of 10^{-8}. This indicates that the diurnal stress at the surface of Io is mainly stored elastically.

The Beta-functions listed in the stress equations illustrate the dependence of the diurnal stress on the Love numbers, $h_{2,e}$ and $l_{2,e}$ or $h_{2,j}$ and $l_{2,j}$, and the colatitude θ. The equations of the Beta-

functions are defined as:

$$\beta_{2,0}^{\theta\theta}(\theta) = \frac{3}{4}(3h_{2,e} - 10l_{2,e})\cos(2\theta) + \frac{3}{4}(h_{2,e} - 2l_{2,e}) \tag{3.6}$$

$$\beta_{2,1}^{\theta\theta}(\theta) = \frac{3}{2}(3h_{2,e} - 10l_{2,e})\sin(2\theta)) \tag{3.7}$$

$$\beta_{2,2}^{\theta\theta}(\theta) = -\frac{3}{2}(3h_{2,e} - 10l_{2,e})\cos(2\theta)) + \frac{9}{2}(h_{2,e} - 2l_{2,e}) \tag{3.8}$$

$$\beta_{2,0}^{\phi\phi}(\theta) = \frac{3}{4}(3h_{2,e} - 8l_{2,e})\cos(2\theta) + \frac{3}{4}(h_{2,e} - 4l_{2,e}) \tag{3.9}$$

$$\beta_{2,1}^{\phi\phi}(\theta)\frac{3}{2}(3h_{2,e} - 8l_{2,e})\sin(2\theta)) \tag{3.10}$$

$$\beta_{2,2}^{\phi\phi}(\theta) - \frac{3}{2}(3h_{2,e} - 8l_{2,e})\cos(2\theta)) + \frac{9}{2}(h_{2,e} - 4l_{2,e}) \tag{3.11}$$

$$\beta_{2,1}^{\theta\phi}(\theta)3l_{2,e}\sin(\theta) \tag{3.12}$$

$$\beta_{2,2}^{\theta\phi}(\theta)3l_{2,e}\cos(\theta) \tag{3.13}$$

3.2.2. VISCOELASTIC STRESSES

This section describes the equations used to calculate the viscoelastically-induced stresses at the surface. The magnitude of the viscoelastic stress is only dependent on the relaxation times that build op the viscoelastic response (Jara Orué, 2016). The viscoelastic stresses can be described as follows:

$$\begin{aligned}\sigma_{\theta\theta}^{v} = &\frac{1}{2}\frac{n^2 R\mu}{g_0}\frac{1}{\sqrt{1+\Lambda^2}}\sum_{j=1}^{M}\left(\frac{1}{\sqrt{1+\Gamma_j^2}}\left\{-6e\beta_{2,0}^{\theta\theta,j}(\theta)\cos\left(nt - \angle\Gamma_j + \angle\Lambda\right)\right.\right.\\ &+4e\beta_{2,2}^{\theta\theta,j}(\theta)\sin(2\phi)\sin\left(nt - \angle\Gamma_j + \angle\Lambda\right)\\ &+3e\beta_{2,2}^{\theta\theta,j}(\theta)\cos(2\phi)\cos\left(nt - \angle\Gamma_j + \angle\Lambda\right)\\ &\left.\left.+4\sin(\varepsilon)\beta_{2,1}^{\theta\theta,j}(\theta)\left[\cos(\phi)\sin\left(\varpi + nt - \angle\Gamma_j + \angle\Lambda\right)\right]\right\}\right)\end{aligned} \tag{3.14}$$

$$\begin{aligned}\sigma_{\phi\phi}^{v} = &\frac{1}{2}\frac{n^2 R\mu}{g_0}\frac{1}{\sqrt{1+\Lambda^2}}\sum_{j=1}^{M}\left(\frac{1}{\sqrt{1+\Gamma_j^2}}\left\{-6e\beta_{2,0}^{\phi\phi,j}(\theta)\cos\left(nt - \angle\Gamma_j + \angle\Lambda\right)\right.\right.\\ &+4e\beta_{2,2}^{\phi\phi,j}(\theta)\sin(2\phi)\sin\left(nt - \angle\Gamma_j + \angle\Lambda\right)\\ &+3e\beta_{2,2}^{\phi\phi,j}(\theta)\cos(2\phi)\cos\left(nt - \angle\Gamma_j + \angle\Lambda\right)\\ &\left.\left.+4\sin(\varepsilon)\beta_{2,1}^{\phi\phi,j}(\theta)\left[\cos(\phi)\sin\left(\varpi + nt - \angle\Gamma_j + \angle\Lambda\right)\right]\right\}\right)\end{aligned} \tag{3.15}$$

$$\begin{aligned}\sigma_{\theta\phi}^{v} = &\frac{1}{2}\frac{n^2 R\mu}{g_0}\frac{1}{\sqrt{1+\Lambda^2}}\sum_{j=1}^{M}\left(\frac{1}{\sqrt{1+\Gamma_j^2}}\right.\\ &\times\left\{8e\beta_{2,2}^{\theta\phi,j}(\theta)\cos(2\phi)\sin\left(nt - \angle\Gamma_j + \angle\Lambda\right)\right.\\ &-6e\beta_{2,2}^{\theta\phi,j}(\theta)\sin(2\phi)\cos\left(nt - \angle\Gamma_j + \angle\Lambda\right)\\ &\left.\left.4\sin(\varepsilon)\beta_{2,1}^{\theta\phi,j}(\theta)\left[\sin(\phi)\sin\left(\varpi + nt - \angle\Gamma_j + \angle\Lambda\right)\right]\right\}\right)\end{aligned} \tag{3.16}$$

where Γ_j is the dimensionless ratio between the mean motion (n) and the inverse relaxation time ($-s_j$) and the Beta-functions are defined as in Equations 3.6 through 3.13, with the elastic Love numbers, $h_{2,e}$ and $l_{2,e}$, substituted for the modal Love numbers, $h_{2,j}$ and $l_{2,j}$.

3.2.3. Diurnal Stresses on Io

In this section, the previously discussed equations for calculating the diurnal stresses at the surface will be applied to Io. The calculations make use of the interior and tidal Love numbers as described in Section 3.1 and Table 3.2, respectively. Table 3.3 provides the other parameters necessary for calculating the diurnal stresses. The value for the argument of periapsis, ϖ, is not relevant as it is only of influence when the obliquity is a non-zero value. Figure 3.1 illustrate the stresses $\sigma_{\theta\theta}$, $\sigma_{\phi\phi}$, and $\sigma_{\theta\phi}$ at perijove. Auxiliary figures of the three components of the normal stress over the period of one orbit can be seen in Section A.2.

Table 3.3: The radius, orbital parameters and rotational parameters of Io used in the diurnal stress calculations. Radius is obtained from Anderson et al. (2001), rest of the parameters are obtained from NASA (2013).

Parameter	Symbol	Value
Mean radius	R	1821.6 km
Mean motion	n	$4.1092 \cdot 10^{-5}$ rad/s
Surface gravity	g_0	1.796 m/s^2
Eccentricity	e	0.0041
Obliquity	ε	0 degrees

Figure 3.1 illustrates that there is a significant phase lag between the elastic and viscoelastic components of each of the normal stresses. The maximum tensile stress of the elastic component for $\sigma_{\theta\theta}$ occurs approximately a quarter orbit before and after perijove, while the maximum tensile stress for the viscoelastic component occurs approximately at perijove and apojove. For $\sigma_{\phi\phi}$, the maximum tensile stress of the elastic component occurs approximately at perijove and apojove. In accordance with the phase lag, the maximum of the tensile stress of the viscoelastic component occurs approximately a quarter orbit before and after perijove. Similar to $\sigma_{\theta\theta}$, the maximum tensile stress of the elastic component for $\sigma_{\theta\phi}$ occurs approximately a quarter orbit before and after perijove, while the maximum tensile stress for the viscoelastic component occurs approximately at perijove and apojove. The phase lag between the elastic and viscoelastic stresses is roughly a quarter orbit for the three components. This phase lag can be calculated as follows:

$$\angle\Gamma_j = \arctan\left(\Gamma_j\right) = \arctan\left(\frac{n}{-s_j}\right) \tag{3.17}$$

Although each relaxation mode contributes to phase lag between the elastic and viscoelastic stresses, not all relaxation modes contribute equally. In the case of Io, with the tidal response in Table 3.2, relaxation mode 3 has the largest influence on the phase lag at a value of 86 degrees. This relaxation mode has the largest influence due to it having a low value for the inverse relaxation time s_j and relatively high values for the modal Love numbers. The relationships between s_j and the stress and the Love numbers and stress originate from Equations 3.15 and 3.16.

The elastic stress is significantly larger than the viscoelastic stress for all three components. The maximum viscoelastic stress is over 29 times smaller than the maximum elastic stress for all components. For example, the maximum elastic stress of $\sigma_{\theta\theta}$ is over 2.28 MPa, while the viscoelastic stress is just 0.08 MPa. As previously mentioned, this is due to the majority of the stress being stored elastically since Λ is of the order of 10^{-8}, much lower than 0.1.

As can be seen in Figure 3.1, the sign of the shear stress depends on which side of the equator is being examined. It can also be seen that the shear stress is zero at the equator. This shows that, besides having a strong longitudinal dependence, the shear stress $\sigma_{\theta\phi}$ also has a strong latitudinal

dependence. This is similar to the normal stress $\sigma_{\phi\phi}$ but in contrast to the normal stress $\sigma_{\theta\theta}$, which mainly depends on its meridian.

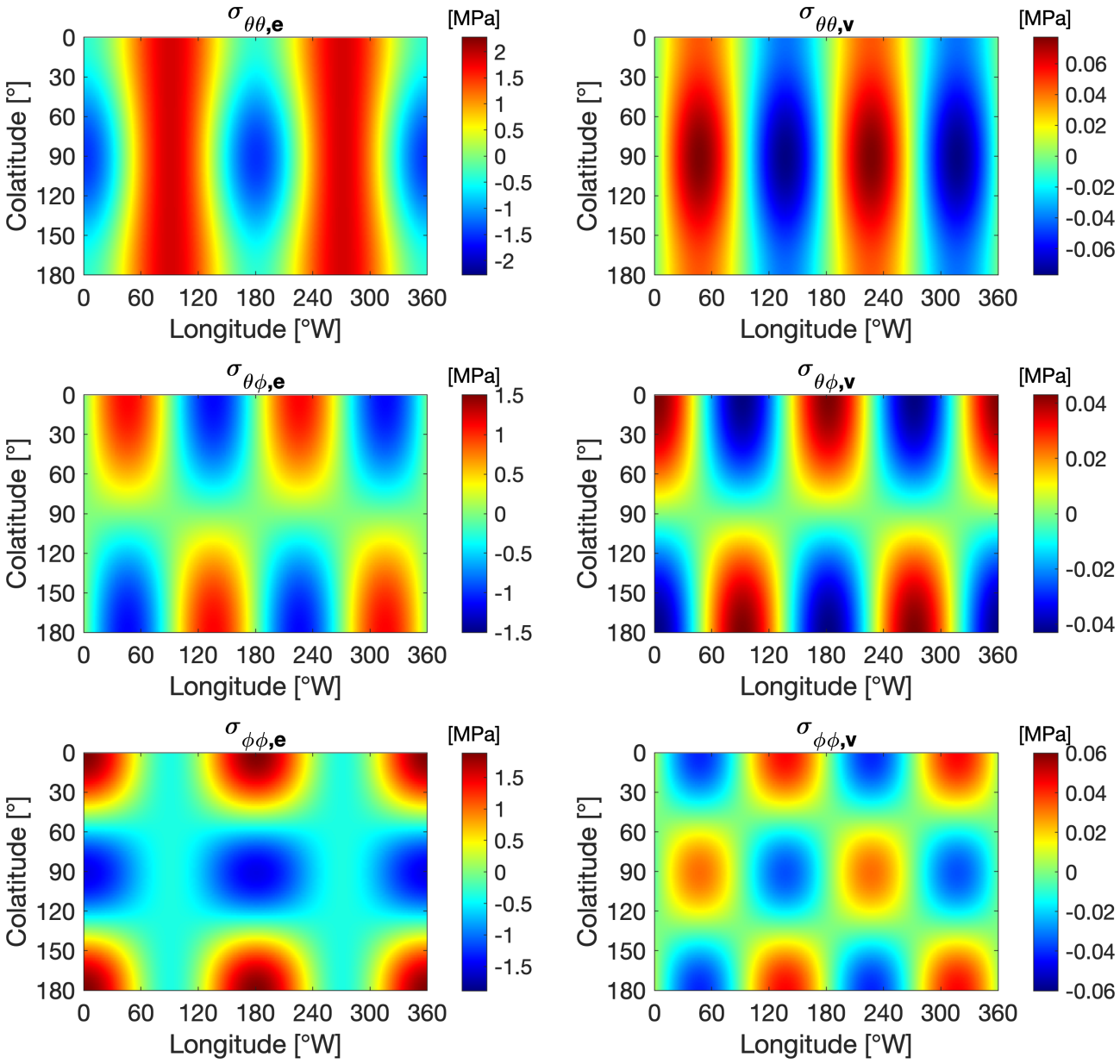

Figure 3.1: The elastic and viscoelastic components of the normal stresses $\sigma_{\theta\theta}$, $\sigma_{\theta\phi}$, and $\sigma_{\phi\phi}$ on the surface Io at perijove.

3.3. Principal Stresses

This section discusses the stresses along the principal axes. The principal axes are defined as oriented so that there are no shear stresses on a surface element (Turcotte and Schubert, 2002). This results in the stresses along these axes being defined at a local maximum. The stresses along these axes are referred to as the principal stresses, σ_1 and σ_2. The principal stresses are used to describe the orientation and magnitude at a point on Io's surface. This allows for determining which direction the tensile stresses act at any point on the surface and its magnitude, allowing for a convenient comparison between the stress on Io's surface and its volcanic distribution.

There are two methods to determine the principal stresses, σ_1 and σ_2. In the first method, the principal stresses can be calculated using $\sigma_{\theta\theta}$, $\sigma_{\phi\phi}$, and $\sigma_{\theta\phi}$ as follows (Turcotte and Schubert, 2002):

$$\sigma_1 = \frac{\sigma_{\theta\theta} + \sigma_{\phi\phi}}{2} + \sqrt{\frac{\left(\sigma_{\theta\theta} - \sigma_{\phi\phi}\right)^2}{4} + \sigma_{\theta\phi}^2} \tag{3.18}$$

$$\sigma_2 = \frac{\sigma_{\theta\theta} - \sigma_{\phi\phi}}{2} + \sqrt{\frac{\left(\sigma_{\theta\theta} - \sigma_{\phi\phi}\right)^2}{4} + \sigma_{\theta\phi}^2} \tag{3.19}$$

The orientation of the principal axes are derived from the orientation angle ϑ. ϑ is the angle between the original axes and the principal axes and is calculated as follows (Turcotte and Schubert, 2002):

$$\tan(2\vartheta) = \frac{2\sigma_{\theta\phi}}{\sigma_{\theta\theta} - \sigma_{\phi\phi}} \tag{3.20}$$

The second method makes use of the fact that the principal stresses are the eigenvalues of the stresses $\sigma_{\theta\theta}$, $\sigma_{\phi\phi}$, and $\sigma_{\theta\phi}$. The direction of the principal axes is determined using the corresponding eigenvectors. This method is particularly useful due to its easy implementation in MATLAB. The first method is used as a verification tool.

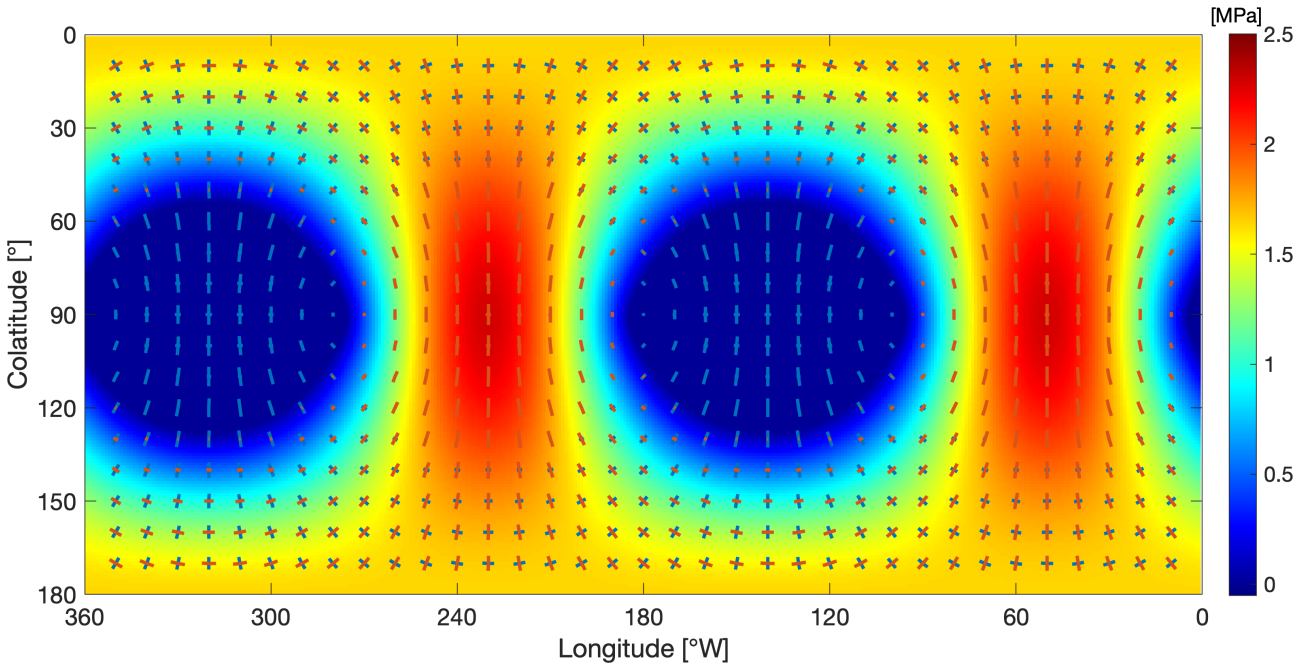

Figure 3.2: The tensile stress at the surface of Io at the point of maximum tensile stress (approximately 103 degrees after apojove). Red lines indicate tension, blue lines indicate compression.

Figure 3.2 illustrates the tensile surface stress at the point of maximum tensile stress. This map is generated by taking the magnitude of the most tensile principal component, if both principal

components are compressive the tensile stress is equal to zero. The lines on this figure indicate the directions of the principal stresses, with the red lines indicating tensile stresses and blue lines indicating compressive stresses. Figure 3.3 illustrates the tensile surface stress at intervals of one-eighth of an orbit. The maximum tensile stress occurs approximately 77 degrees before perijove and a secondary maximum occurs approximately 83 degrees after perijove. The maximum compressive stress occurs approximately 77 degrees before apojove and a secondary maximum occurs approximately 81 degrees after perijove. The direction of the principal stresses is consistent with those determined by Bart et al. (2004).

The spatial pattern of the tensile stress over the period of an orbit is compared to the spherical harmonics from Section 2.3 in Section 4.1 and the direction of the tensile stresses along the principal axes are compared to the direction of the reconstructed curves from Section 2.4 in Section 4.2.

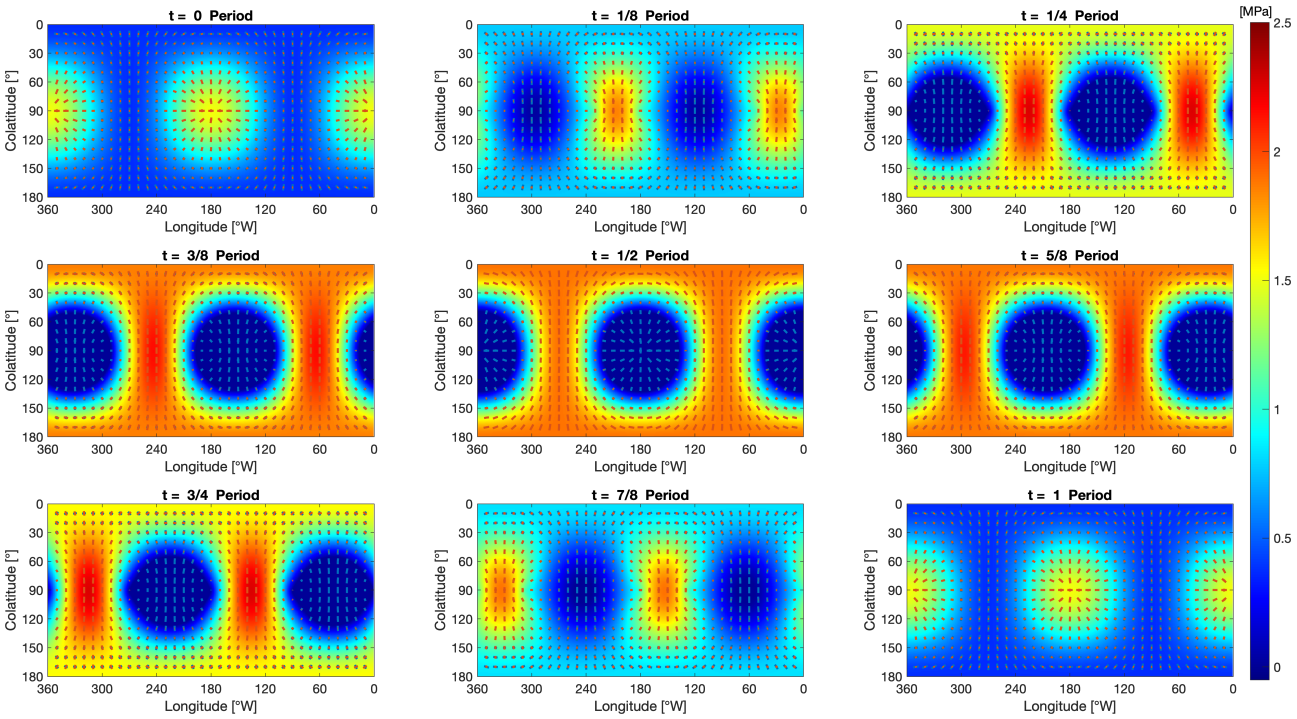

Figure 3.3: A map of the tensile stress over the period of one orbit, in time steps of one eighth of an orbit. Lines indicate the directions of the stress. Red lines indicate tension, blue lines indicate compression.

4
COMPARISON OF THE TENSILE STRESS AND THE VOLCANIC DISTRIBUTION

In Chapter 2, significant density variations in Io's volcanic distribution, on a global scale, using spherical harmonics were found. Similarly, on a local scale, it was found that chains of volcanic centers, reconstructed using the curve reconstruction algorithm, were orientation in significant directions.

In Chapter 3, the tensile diurnal stress was analyzed as a potential mechanism behind Io's volcanic distribution. The direction of the tensile stress as well as the spatial pattern is determined along Io's orbit.

In this chapter, the tensile stress and the volcanic distribution are compared. First, global effects are analyzed by comparing the spatial pattern of the tensile stress to the density of the volcanic centers using spherical harmonics. Second, local effects are analyzed by comparing the directions of the reconstructed volcanic chains to the direction of the tensile stresses.

4.1. COMPARING STRESS AND VOLCANIC CENTERS USING SPHERICAL HARMONICS

This section describes the comparison between the tensile diurnal stress field and the spherical harmonic representation of Io's volcanic distribution. It is hypothesized that the tensile stress will result in fractures in the lithosphere, allowing for volcanism to occur. As the stress field changes along Io's orbit, the comparison is performed at multiple intervals along the orbit.

4.1.1. METHODOLOGY

To compare the diurnal stress field and the volcanic distribution using spherical harmonics, the stress field must first be converted into spherical harmonic coefficients. As the stress field is not made up of a discrete number of points but a 360 by 180 degree field, the method of determining the harmonic coefficients in Section 2.3 is not applicable. For the stress field the method from Sneeuw (1994) is used. This is a two step method as described below:

$$\left.\begin{matrix} A_m(\theta_i) \\ B_m(\theta_i) \end{matrix}\right\} = \frac{1}{L(1+\delta_{m0}+\delta_{mL})} \sum_{j=0}^{2L+1} f(\theta_i,\phi_j) \left\{\begin{matrix} \cos m\phi_j \\ \sin m\phi_j \end{matrix}\right. \tag{4.1}$$

$$\left.\begin{matrix} C_{lm} \\ S_{lm} \end{matrix}\right\} = \sum_{i=1}^{N} (-1)^m \sqrt{\frac{(2-\delta_{0m})(2l+1)(l-m)!}{(l+m)!}} P_{lm}(\cos\theta_i) \left\{\begin{matrix} A_m(\theta_i) \\ B_m(\theta_i) \end{matrix}\right. \tag{4.2}$$

where L is the maximum spherical harmonic degree and f is the field to be analyzed.

The normalization of Equation 4.2 is defined similarly to that of the method described in Section 2.3. The difference is that the method in Section 2.3 is defined per unit area, while the stress is already defined per unit area. This slight difference is inconsequential for the comparison, as the harmonic coefficients are equalized when the correlation is calculated.

To verify that this method produces the proper spherical harmonic coefficients, a field is reconstructed from the calculated harmonic coefficients using Equation 2.8. The results of this verification are illustrated in Figure 4.1. As can be seen in these graphs, they are nearly identical and

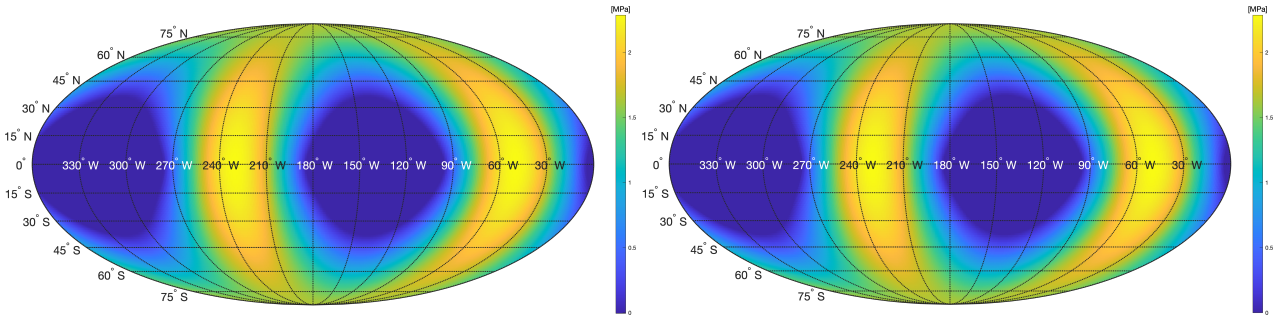

(a) (b)

Figure 4.1: (a) The original tensile stress field at maximum tensile stress. (b) The reconstructed field using the spherical harmonic coefficients. Field is truncated at degree $l = 179$.

are both scaled the same. The maximum tensile stress of the original field is equal to 2.2850 MPa, while the reconstructed field has a maximum of 2.2849 MPa, within 0.007% of each other. This insignificant difference is caused by truncation.

The spherical harmonic coefficients of the stress field and volcanic distribution are compared by calculating the correlation coefficient. The correlation coefficients are calculated for each degree as follows (Johnson and Richards, 2003; Richards et al., 1988):

$$r_l = \frac{\sum_{m=0}^{l} (C_{lm}G_{lm} + S_{lm}H_{lm})}{\sqrt{\sum_{m=0}^{l} (C_{lm}^2 + S_{lm}^2) \sum_{m=0}^{l} (G_{lm}^2 + H_{lm}^2)}} \tag{4.3}$$

where C_{lm} and S_{lm} are the spherical harmonic coefficients of the first set and G_{lm} and H_{lm} are the coefficients of the second set.

The correlation has a range between 1 and -1. A value of 1 indicates a maximum positive correlation, while a value of -1 indicates maximum anti-correlation and a value of 0 indicates no correlation at all. To determine the significance of the correlation a two-tailed Student-t normal distribution, with $2l$ degrees of freedom, is used (Press et al., 2007).

$$r_l = \pm t_\alpha \sqrt{\frac{1}{2l + t_\alpha^2}} \tag{4.4}$$

where α is the required significance level and t_α is the parameter required to obtain this significance level.

4.1.2. Results

Using the spherical harmonic coefficients of Io's volcanic distribution and the coefficients from the diurnal stress field, the correlation between the distribution and stress is determined, using Equation 4.3. As the magnitude and pattern of the stress changes along Io's orbit, the correlation is calculated over the period of one Ionian orbit, in time steps of 1 degree. For the purpose of this analysis, only the tensile stress component of the principal stresses is used. This is due to the hypothesized relation between tensile stress and volcanism.

The results are discussed by comparing the correlation for Io's volcanic distribution with correlation for Monte Carlo analyses, with a random distribution and a clustered random distribution. Figure 4.2 illustrates the correlation between the tensile stress and Io's volcanic distribution as well as for the randomly distributed data sets. Figure 4.3 illustrates the correlation between the tensile stress and the clustered randomly distributed data sets and, once again, Io's volcanic distribution. The Monte Carlo analyses both contain 10,000 generated data sets with 794 data points in each set, with 794 being the number of volcanic centers in Io's distribution.

As can be seen in these figures, the correlation is only determined for degree 2. This is due to the equations for the diurnal stresses (Equations 3.1 to 3.3) being dependent only on degree 2 components. For degree 2, Io's volcanic distribution shows a peak of over 95% significant anti-correlation with the tensile stress at approximately 30 degrees before apojove. A secondary peak is apparent around 30 degrees before perijove. This secondary peak shows a slightly lower positive correlation, just under 95% significant.

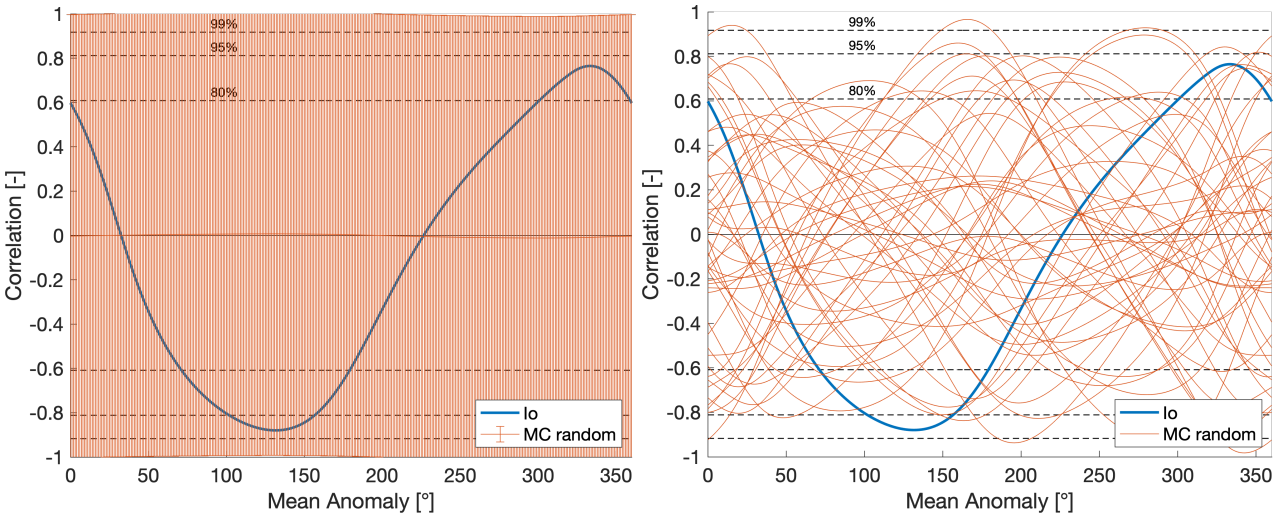

(a) (b)

Figure 4.2: Correlation between the spherical harmonic coefficients of tensile diurnal stress and Io's volcanic distribution for degree 2 in blue. Orange areas (a) indicate 3-sigma confidence interval and orange lines (b) represent 50 randomly selected samples for a Monte Carlo analysis using 10,000 sets of 794 randomly generated data points. Apojove is at a mean anomaly 0°. Perijove is at a mean anomaly of 180°.

First, the correlation between the tensile stress and Io's distribution is compared to the correlation for a randomly distributed Monte Carlo analysis. As illustrated in Figure 4.2, the behavior for the random distribution varies widely. The 3-sigma confidence interval fills the entire correlation range between -1 to 1. This indicates that there is a significant variation between the sample random distributions, as illustrated in Figure 4.2a. This figure shows fifty of the sample distributions. As seen in the figures, the correlation for Io's distribution completely falls within the random distributions. Thus, these figures show that the correlation between the tensile stress and Io's volcanic distribution can be explained by a random distribution.

Next, the correlation between the tensile stress and Io's distribution is compared to the correlation for the clustered randomly distributed Monte Carlo analysis. As seen in Figure 4.3a, the results of the Monte Carlo analysis for a clustered random distribution are fairly different from the results for a completely random distribution. Unlike for a random distribution, where the mean value is approximately zero, the mean correlation for a clustered distribution is at a maximum near perijove and a minimum near apojove. This behavior is also quite opposite to Io's distribution, as the maximum correlation is at apojove as opposed to 30 degrees before perijove and the maximum anti-correlation is at perijove, as opposed to 30 degrees before apojove. The correlation for Io's distribution does not fit entirely within the 3-sigma confidence interval of the clustered random distribution. However, as seen in Figure 4.2b, some samples match the location of the maximums and shape of the correlation with Io's distribution.

Overall, it can be said that the correlation between the tensile stress and Io's volcanic distribution can be explained by a random distribution. However, outliers of the correlation for a clustered random distribution can also match the observed behavior.

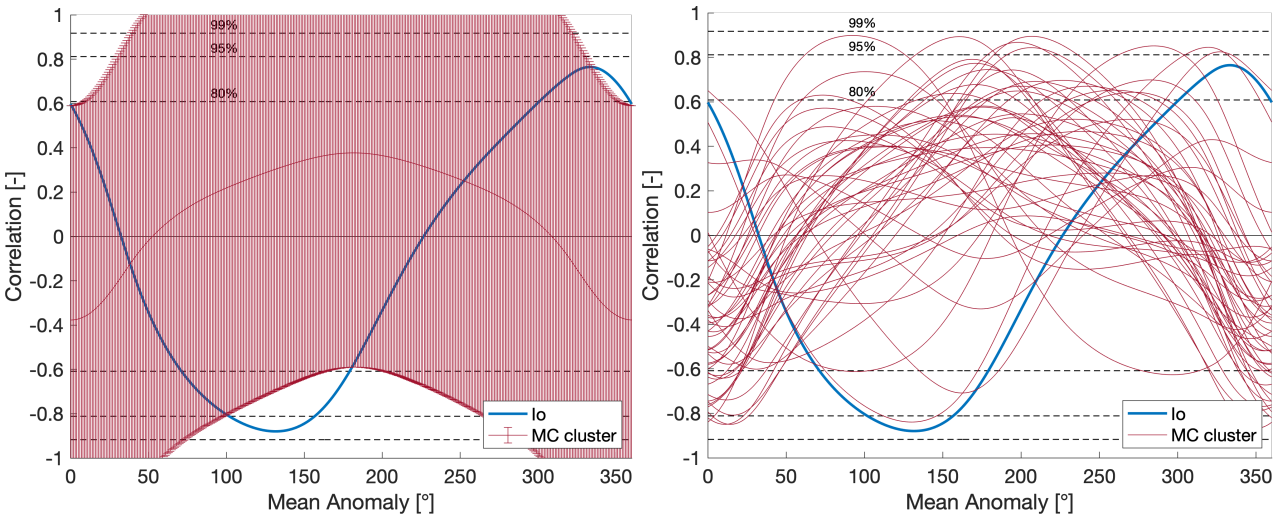

(a) (b)

Figure 4.3: Correlation between the spherical harmonic coefficients of tensile diurnal stress and Io's volcanic distribution for degree 2 in blue. Red areas (a) indicate 3-sigma confidence interval and red lines (b) represent 50 randomly selected samples for a Monte Carlo analysis using 10,000 sets of 794 clustered randomly generated data points. Apojove is at a mean anomaly 0°. Perijove is at a mean anomaly of 180°.

4.2. Comparing Stress and Volcanic Centers using Curve Reconstruction

This section describes the comparison between the direction of the tensile diurnal stresses and the reconstructed curves of Io's volcanic distribution. This allows for determining if volcanic chains are aligned with the direction of the tensile stress. It is hypothesized that cracks in the lithosphere are propagated along the direction of the stress, allowing volcanism to occur. Similar to the comparison with the spherical harmonics, the comparison is performed at multiple intervals along the orbit.

4.2.1. Methodology

To compare the diurnal stresses and the reconstructed curves of Io's volcanic distribution, the direction the stress and the direction of the reconstructed curves are compared. This comparison is performed at the center of each curve segment. Figure 4.4 illustrates the tensile surface stress map, as discussed in Section 3.3, with the directions of the principal stresses at the middle points of the reconstructed curve segments.

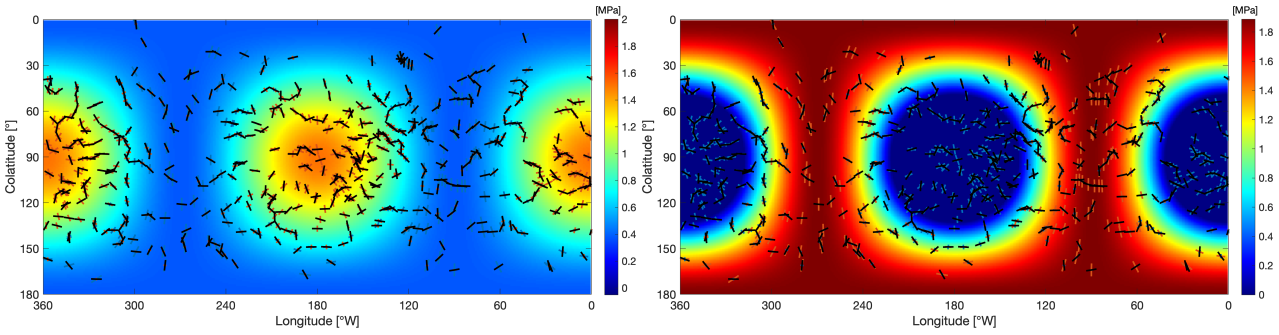

(a) (b)

Figure 4.4: The tensile stress at the surface of Io at apojove (a) and at perijove (b), with the directions of the principal stresses at the mid points of the reconstructed curve segments. Red lines indicate tension, blue lines indicate compression, and black lines indicated reconstructed curve segments.

As it is hypothesized that the tensile stress is directly related to the patterns in Io's volcanism, only the tensile components of the principal stresses are considered. To compare the direction of the tensile stress and the curve segments, the difference in heading angle is determined for each curve segment. As illustrated in Figure 4.5, there are two different cases of stress to be considered. In the first case, only one of the two principal stresses is tensile (Figure 4.5a). In the second case, both principal stresses are tensile (Figure 4.5b).

In the first case, the angle between the curve segment and tensile stress is calculated. As the direction of the curve segments is arbitrary, there is no positive or negative direction. Therefore, the difference in direction is normalized between -90 and 90 degrees. In the second case, the angle between the curve segment and both the tensile stresses are calculated and the smallest value is used.

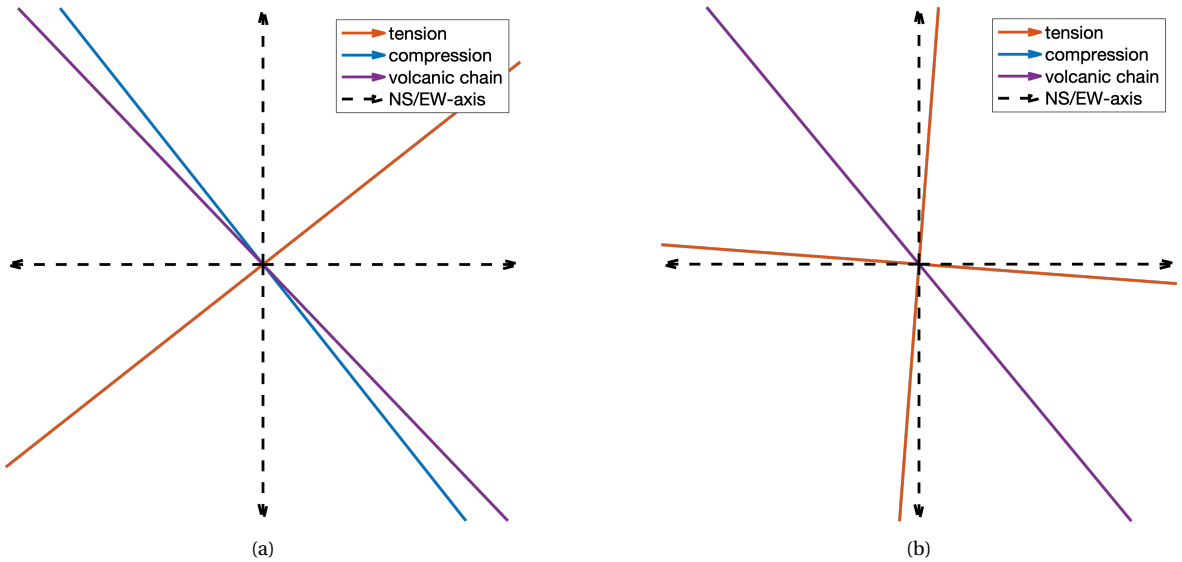

Figure 4.5: The two cases of the principal stresses considered, (a) only one of the principal stresses is tensile (b) both principal stresses are tensile. The orange line indicates the direction of the tensile stresses, the blue line indicates the direction of compressive stresses, the purple line indicates the direction of the curve segment, and the dashed black arrows indicates the vertical north-south (NS) axis and the horizontal east-west (EW) axis.

4.2.2. Results

Using the directions of the tensile stress and the direction of the reconstructed curves of Io's volcanic distribution, the difference in heading angle is determined over a period of one Ionian orbit, in time steps of 1 degree.

Similar to the comparison between the tensile stress and the Io's volcanic distribution using spherical harmonics, the comparison between the direction of the tensile stress and the direction of the reconstructed curves of Io's volcanic distribution, or volcanic chains, is discussed by comparing the difference in heading angle for Io's volcanic distribution with the difference in heading angle for two Monte Carlo analyses. The first Monte Carlo analysis with a random distribution and the second with a clustered random distribution. The Monte Carlo analyses both contain 1,000 generated data sets with 794 data points in each set. The number of data sets is smaller than in the previous section due to the significantly larger computation time per data set.

A good indication of the alignment between the direction of the tensile stress and volcanic chains is the standard deviation of the difference in the heading angle. A lower standard deviation indicates greater alignment as more of the measurements tend towards the median. A higher standard deviation indicates a more evenly spread difference in the heading angle. The standard deviation of the differences in heading angle for Io's volcanic chains as well as for the random and clustered Monte Carlo analyses are illustrated in Figure 4.6a and Figure 4.6b, respectively. As seen in these

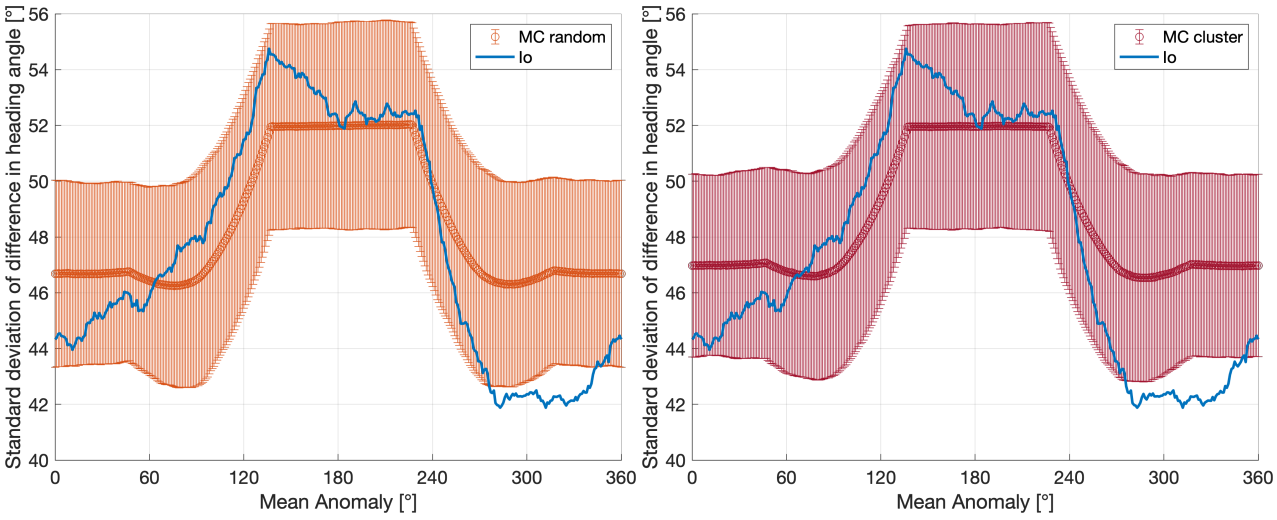

(a) (b)

Figure 4.6: The standard deviation of the difference in heading angle between the direction of the tensile stress and the direction of the volcanic chains, in blue. The orange area (a) indicates 3-sigma confidence interval of the results for a random distribution Monte Carlo analysis, and the red area (b) indicates 3-sigma confidence interval of the results for a clustered random distribution Monte Carlo analysis.

figures, the standard deviation for Io is at a minimum near apojove and is at a maximum near perijove. This indicates that the direction of the stress and volcanic chains align better near apojove.

In Figure 4.6a, the standard deviation of the difference in heading angle for Io's volcanic distribution is compared to a random distribution. As seen in this figure, the standard deviation for Io's distribution fits within the 3-sigma confidence interval of the standard deviation for a random distribution, with the exception of a region between 276 and 344 degrees. In this region, Io has a lower standard deviation than expected for a random distribution, with the maximum difference occurring approximately 30 degrees before apojove. This may imply that the stress and volcanic chains are more aligned than expected for a random distribution in this region.

Figure 4.6b compares the standard deviation of the difference in heading angle for Io's volcanic distribution with a clustered random distribution. As seen in this figure, the 3-sigma confidence interval for a clustered random distribution is similar to that of a random distribution. However, it is offset slightly towards a higher standard deviation. Due to this higher standard deviation, the region of Io's distribution that falls outside the 3-sigma confidence interval increases slightly to between 276 and 352 degrees. The maximum difference still occurs approximately 30 degrees before apojove. Thus, similar to a random distribution, the standard deviation may indicate that around apojove the stress and volcanic chains are more aligned than expected for a clustered random distribution.

As both figures in Figure 4.6 illustrate, the standard deviation is at a maximum approximately 40 degrees before perijove. The maximum is still within the expected 3-sigma confidence interval. However, it is near the maximum value, especially for the clustered distribution.

Figure 4.7 shows histograms for the difference in heading angle at key moments. These histograms are used to confirm that the direction of the tensile stress and volcanic chains align more near apojove and less near perijove, as well as to additionally test the significance of the distribution. The first histogram portrays the difference in heading angle around the minimum standard deviation after apojove, the second histogram portrays the difference near the maximum standard deviation before perijove, and the third histogram portrays the difference near the lowest standard deviation before apojove. As expected, these figures illustrate that stress and volcanic chains are better aligned near apojove than near perijove. However, the figures near apojove also illustrate that

although the standard deviation is lower than expected, it does not result in overtly significant differences between the histogram for Io and those for the clustered and random distribution.

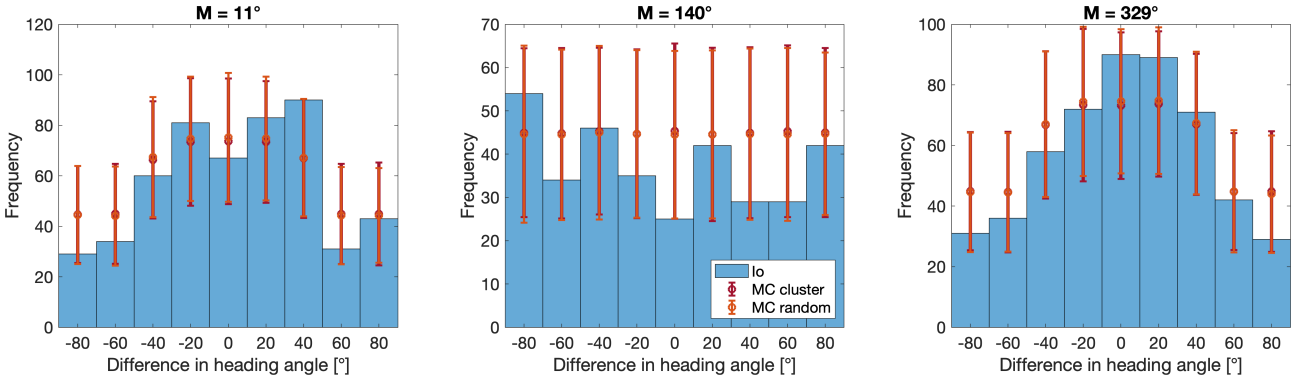

Figure 4.7: Histograms of the differences in heading angles between the direction of the tensile stress and the direction of the volcanic chains at 11 degrees (left), 140 degrees (middle), and 329 degrees (right) after apojove. Blue indicates the results for Io's volcanic distribution, orange indicates 3-sigma confidence interval of the results for a random distribution Monte Carlo analysis, and red indicates 3-sigma confidence interval of the results for a clustered random distribution Monte Carlo analysis.

5
DISCUSSION

In this chapter, the results of the comparison between the tensile diurnal stresses on Io and the volcanic distribution are discussed. First, the comparison using spherical harmonics is discussed. Second, the comparison using the curve reconstruction algorithm is discussed. Finally, the combined results are discussed.

Section 4.1 presented the results of the comparison between the tensile stress and the volcanic distribution using spherical harmonics on a global scale. As seen in this section, the degree 2 correlation between the tensile stress and volcanic distribution shows a strong correlation approximately 30 degrees before apojove and a strong anti-correlation approximately 30 degrees before perijove. This 30 degree offset with respect to the apsides is likely coupled to the 30 degree eastward offset of the volcanic distribution with respect to the tidal axis. This eastward offset was observed in the spherical harmonic analysis of Io's volcanic distribution in Section 2.3, as well as in previous studies by de Kleer and de Pater (2016) and Hamilton et al. (2013).

Besides the 30 degree offset, it is of note that stress and volcanic distribution are over 95% significant anti-correlated near perijove and just under 95% significant correlated near apojove. This observed behavior fits within the confidence interval for the Monte Carlo simulation of a random distribution, and therefore can be explained by a random distribution. The observed behavior does not completely fit within the 3-sigma confidence interval of a Monte Carlo simulation for a clustered random distribution. The mean value for the minimum and maximum correlation are at apojove and perijove, respectively. This does not match the offset of Io's distribution. However, several outliers of a clustered random distribution can still account for the 30 degree offset as well as the correlation near apojove and anti-correlation near perijove. This may indicate that although the correlation for Io's distribution fits within the expected range for a random distribution, the correlation pattern and offset can be partially attributed to the clustering of volcanic centers, although it is still slightly anomalous.

Section 4.2 compared the directions of the tensile stress and direction of reconstructed volcanic chains on a local scale. The difference between the direction of the stress and volcanic chains is referred to as the difference in the heading angle. The significance of the difference in heading angle is investigated by determining the standard deviation of the difference in heading angle over the period of an orbit. The results show that the standard deviation for Io fits more with a random distribution than a clustered random distribution.

The results in Section 4.2 show that the standard deviation of the difference in heading angle for Io's volcanic distribution is statistically significantly lower than expected for a random distribution between a mean anomaly of 276 and 344 degrees. The maximum deviation between Io's distribution and a random distribution occurs approximately 30 degrees before apojove, at a mean anomaly of 330 degrees. Similarly, the lower standard deviation of Io before apojove is also statistically significant with respect to a clustered random distribution. The region that is statistically significant is slightly larger between a mean anomaly of 276 and 352 degrees. The maximum deviation is again located approximately 30 degrees before apojove. The 3-sigma confidence interval for the standard deviation of a clustered random distribution near apojove is located slightly higher than for that of a random distribution and Io's results. This is due to the directions of the volcanic chains being more disorganized in a clustered random distribution below chain lengths of approximately

100 km than for Io and a random distribution. This skews the standard deviation upwards. This indicates that, on a local scale, the results for Io more closely match that of a random distribution than a clustered distribution. However, the dip approximately 30 degrees before apojove implies a statistically significant alignment between the direction of the tensile stress and volcanic chains.

Both the global scale results and the local scale results have a 30 degree offset with respect to the apsides. On a global scale, the correlation between the tensile stress field and Io's volcanic distribution is at a maximum approximately 30 degrees before apojove. On a local scale, the direction of the tensile stress and the direction of the reconstructed volcanic chains are in statistically significant alignment around 30 degrees before apojove. This implies that the 30 degree offset is of significance. According to Hamilton et al. (2013), the 30 degree offset could be caused by two other phenomena besides stress. It could also be attributed to a faster-than-synchronous rotation of Io or a missing component of Io's tidal response.

No evidence has been found that Io has a faster-than-synchronous or non-synchronous rotation (Schenk et al., 2001). A faster-than-synchronous rotation would, over geological time scales, cause Io to rotate away from its tidal axis. This would imply that volcanic centers formed according to the asthenospheric heating model would shift eastward causing the observed offset (Schenk et al., 2001). This can also explain the degree 2 correlation, however, it cannot provide an explanation for the significant alignment between the direction of the stress and volcanic chains. A faster-than-synchronous rotation can also induce stresses in the lithosphere (Bart et al., 2004), however, these stresses should not change the conclusion.

A model developed by Tyler et al. (2015) includes the tidal response of a partially molten interior layer, a magma ocean as derived by Khurana et al. (2011). It is currently thought that the tidal dissipation pattern is related to the volcanic distribution (e.g. Hamilton et al., 2013; Tyler et al., 2015; Tackley, 2001). Regions of higher dissipation would result in more volcanic activity. However, no conclusive evidence has been found to support this (Hamilton et al., 2013; Kirchoff et al., 2011; de Kleer and de Pater, 2016; Tyler et al., 2015). Similarly, no conclusive evidence for stress resulting in volcanic activity on Io has been found. If the dissipation pattern influenced the volcanic distribution, then volcanic centers formed according to the tidal dissipation of the model from Tyler et al. (2015) would also result in a similar correlation with the tensile stress as seen in Section 4.1, including the 30 degree offset. However, the tidal response of a partially molten interior layer would only result in a small offset of the stress pattern, not a 30 degree offset. Therefore, an additional tidal response component would not yield the offset in the maximum alignment between the direction of the stress and the volcanic chains.

As the offset is approximately the same for both the correlation and alignment, a magma ocean is unlikely to be the mechanism behind the 30 degree offset. A faster-than-synchronous rotation can explain the 30 degree offset, but not the alignment between the direction of the stress and the volcanic chains itself.

The local scale results indicate that the orientations of the volcanic chains are consistent with the orientation of the tensile stress. However, the correlation between the tensile stress field and volcanic distribution fits with a random distribution and outliers of a clustered random distribution, indicating that tensile stress alone is not enough to explain the volcanic distribution. These results are comparable to a study on the ridge formation due to tidal stresses on Io by Bart et al. (2004). In this thesis, Bart et al. (2004) found that the orientations of the ridges are consistent with tidal stresses, however, tidal stresses alone cannot explain all the aspects of ridge formation. In the case of volcanism, the mechanism behind the clustering of the volcanic centers may play an important role as well.

6

CONCLUSION AND RECOMMENDATIONS

As stated at the beginning of this thesis, the main purpose of this thesis was to investigate if the tensional stresses on Io play a significant role in the formation of the volcanic centers. This was investigated by examining the stress and volcanism on a local and a global scale.

On a local scale, it was investigated if chains of Io's volcanoes follow the directions of the tensile stresses. Using the curve reconstruction algorithm, chains of volcanic centers were reconstructed. Unlike on Earth, no significant amount of chains were found. However, the chains that were determined showed potential alignment. When compared to the direction of the tensile stress, it was found that there is a statistically significant alignment between the direction of the tensile stress and the direction of the volcanic chains roughly 30 degrees before apojove. This significant alignment deviates from a random distribution and cannot be attributed to the clustering of volcanic centers.

On a global scale, it was investigated if the locations of maximum tensile stress coincide with the locations of maximum volcanic activity. The spherical harmonic analysis of the volcanic distribution found a statistically significant degree 2 signal centered around the equator with a 30 degree eastward offset from the tidal axis. This eastward offset is also present in previous studies on the volcanic distribution. When compared to the tensile stress field, it was found that there is a significant correlation between the degree 2 spherical harmonics of the tensile stress field and the volcanic distribution. This correlation can, however, be attributed to a random distribution and outliers of a clustered distribution. Similar to the local scale results, the global scale results have a 30 degree offset with respect to the apsides.

The found 30 degree offset in the maximum alignment and maximum correlation with respect to the apsides is similar to 30 degree offset in the volcanic distribution with respect to the tidal axis. Besides stress, it is thought that a magma ocean or faster than synchronous rotation can cause the offset. A potential magma ocean can account for the 30 degree offset in the global results. However, it is unlikely to account for the 30 degree offset in the local results. Similarly, a faster than synchronous rotation can result in the 30 degree offset seen in both the local and global results. However, it cannot account for the statistically significant alignment between the direction of stress and volcanic chains.

A clustered random distribution can also result in the observed degree 2 correlation. However, it cannot result in the observed alignment between the direction of stress and volcanic chains. Clustering is thought to be the result of multiple volcanic centers being fed from the same source or phenomena such as the clustering of mantel plumes.

In conclusion, it can be said that the tensile diurnal stress on Io plays a role in the formation of volcanic centers. However, it is unlikely that it is the only contributing factor nor is it the driving mechanism behind the volcanic distribution. Other phenomena, such as the mechanisms behind the clustering of volcanic centers or potential faster than synchronous rotation, are likely to play a significant role in Io's immense volcanism.

In addition to the conclusion to the thesis presented above, the research in this thesis has also raised several topics that could be the subject of future research:

- **Perform the curve reconstruction analysis per hemisphere or in specific regions instead of globally**

As was seen in the histograms of Figure 2.4 and the spherical harmonic field in Figure 2.9, volcanic centers are concentrated in several regions. It may prove insightful to analyze the relationship between stress and volcanism in regions of higher and lower concentrations. This could allow for determining if stress has a higher or lower influence in regions of higher concentrations. It could also shed light on if stress complements potential clustering or if they are two separate mechanisms, i.e. magma plumes cause clustered volcanic centers and fractures in the lithosphere in other regions cause the rest of the volcanism.

- **Combining the curve reconstruction algorithm with the mechanics of fracture propagation**

The current curve reconstruction analysis only compares the direction of the curve segment with the direction of the tensile stress. It could prove insightful to investigate the difference in how the fractures in the lithosphere should propagate due to tensile stresses according to current theories (e.g. Rittmann, 1962; Han-Shou, 1980; Poinelli, 2017) and how they are propagated according to the curve reconstruction results.

- **Improve the clustered random distribution algorithm**

A clustered random distribution was found to partially match the behavior of the degree 2 correlation between the tensile stress and the volcanic distribution. It could be possible to improve this match by also taking the directions of the tensile stress into account when generating the clustered random data points. So that the generated volcanic centers align form volcanic chains aligned with the direction of the tensile stress. This should allow for the ability to better determine if the mechanism behind the clustering of volcanoes in combination with stress causes the observed volcanic distribution.

- **Analyze different kinds of stress**

In this thesis, the volcanic distribution is compared to tensile diurnal stresses. However, there are stresses that could influence the development of volcanic centers, such as convective stresses (Schenk et al., 2001). In the case of convective stresses, mantle downwellings create compressive stresses. Similarly, mantle upwellings impose tensional stresses due to thinning and stretching of the crust. Regions, where the crust is thinner, could potentially allow more melt and therefore for more volcanism to occur (Kirchoff et al., 2011; Schenk et al., 2001). Thus, investigating other types of stresses might yield additional insight into the role that stresses play in the formation of volcanic centers.

- **Challenge the assumption that the volcanic distribution is representative of Io's global distribution.**

In this thesis and in previous studies (e.g. Hamilton et al., 2013; Davies et al., 2015; de Kleer and de Pater, 2016; Rathbun et al., 2018), it is assumed that the observed volcanic distribution is representative of Io's global volcanic distribution and heat glow. However, even with the inclusion of volcanic eruptions observed by Juno and analyzed by Mura et al. (2020), there is still a scarcity of volcanic activity observed on Io's poles. The current understanding is that this is due to tidal heating primarily taking place in the asthenosphere. More observations of Io, and specifically its polar regions, could shed light on if the lack of observed volcanic activity is due to a lack of observations or if it is due to a lack of activity as assumed. This could be achieved through continued Earth-based observations, additional flybys of Io by the Juno spacecraft, and/or the potential dedicated mission to Io, the Io Volcanic Observer (IVO) by NASA (2020).

BIBLIOGRAPHY

T. C. O'Reilly and G. F. Davies, "Magma transport of heat on Io: A mechanism allowing a thick lithosphere," *Geophysical Research Letters*, vol. 8, no. 4, pp. 313–316, 1981.

D. Turcotte and E. Oxburgh, "Stress accumulation in the lithosphere," *Tectonophysics*, vol. 35, no. 1-3, pp. 183–199, 1976.

M. Segatz, T. Spohn, M. Ross, and G. Schubert, "Tidal dissipation, surface heat flow, and figure of viscoelastic models of Io," *Icarus*, vol. 75, no. 2, pp. 187–206, 1988.

C. W. Hamilton, C. D. Beggan, S. Still, M. Beuthe, R. M. Lopes, D. A. Williams, J. Radebaugh, and W. Wright, "Spatial distribution of volcanoes on Io: Implications for tidal heating and magma ascent," *Earth and Planetary Science Letters*, vol. 361, pp. 272–286, 2013.

A. G. Davies, G. J. Veeder, D. L. Matson, and T. V. Johnson, "Map of Io's volcanic heat flow," *Icarus*, vol. 262, pp. 67 – 78, 2015. [Online]. Available: http://www.sciencedirect.com/science/article/pii/S0019103515003474

A. Mura, A. Adriani, F. Tosi, R. Lopes, G. Sindoni, G. Filacchione, D. Williams, A. Davies, C. Plainaki, S. Bolton *et al.*, "Infrared observations of Io from Juno," *Icarus*, vol. 341, p. 113607, 2020.

K. de Kleer, I. de Pater, E. M. Molter, E. Banks, A. G. Davies, C. Alvarez, R. Campbell, J. Aycock, J. Pelletier, T. Stickel *et al.*, "Io's Volcanic Activity from Time Domain Adaptive Optics Observations: 2013–2018," *The Astronomical Journal*, vol. 158, no. 1, p. 29, 2019.

USGS, "Io Galileo SSI / Voyager Color Merged Global Mosaic 1km," Mar 2012. [Online]. Available: https://astrogeology.usgs.gov/search/map/Io/Voyager-Galileo/Io_GalileoSSI-Voyager_Global_Mosaic_ClrMerge_1km

C. Beggan and C. W. Hamilton, "New image processing software for analyzing object size-frequency distributions, geometry, orientation, and spatial distribution," *Computers & Geosciences*, vol. 36, no. 4, pp. 539–549, 2010.

M. R. Kirchoff, W. B. McKinnon, and P. M. Schenk, "Global distribution of volcanic centers and mountains on Io: Control by asthenospheric heating and implications for mountain formation," *Earth and Planetary Science Letters*, vol. 301, no. 1, pp. 22 – 30, 2011. [Online]. Available: http://www.sciencedirect.com/science/article/pii/S0012821X10007132

T. K. Dey, K. Mehlhorn, and E. A. Ramos, "Curve reconstruction: Connecting dots with good reason," *Computational Geometry*, vol. 15, no. 4, pp. 229–244, 2000.

H. Sigurdsson, B. Houghton, S. McNutt, H. Rymer, and J. Stix, *The encyclopedia of volcanoes*. Elsevier, 2015.

J. D. Anderson, R. A. Jacobson, E. L. Lau, W. B. Moore, and G. Schubert, "Io's gravity field and interior structure," *Journal of Geophysical Research: Planets*, vol. 106, no. E12, pp. 32 963–32 969, 2001.

NASA, "JPL Solar System Dynamics: Planetary Satellite Mean Orbital Parameters," 2013. [Online]. Available: https://ssd.jpl.nasa.gov/?sat_elem

S. J. Peale, P. Cassen, and R. T. Reynolds, "Melting of Io by tidal dissipation," *Science*, vol. 203, no. 4383, pp. 892–894, 1979.

D. L. Turcotte and G. Schubert, *Geodynamics*. Cambridge university press, 2002.

K. de Kleer and I. de Pater, "Spatial distribution of Io's volcanic activity from near-IR adaptive optics observations on 100 nights in 2013–2015," *Icarus*, vol. 280, pp. 405–414, 2016.

W. G. Henning, J. P. Renaud, P. Saxena, P. L. Whelley, A. M. Mandell, S. Matsumura, L. S. Glaze, T. A. Hurford, T. A. Livengood, C. W. Hamilton *et al.*, "Highly Volcanic Exoplanets, Lava Worlds, and Magma Ocean Worlds: An Emerging Class of Dynamic Exoplanets of Significant Scientific Priority," *arXiv preprint arXiv:1804.05110*, 2018.

V. Lainey, J.-E. Arlot, Ö. Karatekin, and T. Van Hoolst, "Strong tidal dissipation in Io and Jupiter from astrometric observations," *Nature*, vol. 459, no. 7249, p. 957, 2009.

A. S. McEwen, L. P. Keszthelyi, R. Lopes, P. M. Schenk, and J. R. Spencer, "The lithosphere and surface of Io," *Jupiter: The Planet, Satellites and Magnetosphere*, pp. 307–328, 2004.

P. Schenk, H. Hargitai, R. Wilson, A. McEwen, and P. Thomas, "The mountains of Io: Global and geological perspectives from Voyager and Galileo," *Journal of Geophysical Research: Planets*, vol. 106, no. E12, pp. 33 201–33 222, 2001.

W. B. Moore, G. Schubert, J. D. Anderson, and J. R. Spencer, "The interior of Io," in *Io after Galileo*. Springer, 2007, pp. 89–108.

K. K. Khurana, X. Jia, M. G. Kivelson, F. Nimmo, G. Schubert, and C. T. Russell, "Evidence of a global magma ocean in Io's interior," *Science*, vol. 332, no. 6034, pp. 1186–1189, 2011.

R. Ernst and D. Desnoyers, "Lessons from Venus for understanding mantle plumes on Earth," *Physics of the Earth and Planetary Interiors*, vol. 146, no. 1-2, pp. 195–229, 2004.

C. B. Connor, F. M. Conway, and H. Sigurdsson, "Basaltic volcanic fields," *Encyclopedia of volcanoes*, pp. 331–343, 2000.

M. O. Garcia, A. J. Pietruszka, and J. M. Rhodes, "A petrologic perspective of Kīlauea volcano's summit magma reservoir," *Journal of Petrology*, vol. 44, no. 12, pp. 2313–2339, 2003.

R. H. Tyler, W. G. Henning, and C. W. Hamilton, "Tidal heating in a magma ocean within Jupiter's moon Io," *The Astrophysical Journal Supplement Series*, vol. 218, no. 2, p. 22, 2015.

G. D. Bart, E. P. Turtle, W. L. Jaeger, L. P. Keszthelyi, and R. Greenberg, "Ridges and tidal stress on Io," *Icarus*, vol. 169, no. 1, pp. 111–126, 2004.

H. M. Jara-Orué and B. L. Vermeersen, "Effects of low-viscous layers and a non-zero obliquity on surface stresses induced by diurnal tides and non-synchronous rotation: The case of Europa," *Icarus*, vol. 215, no. 1, pp. 417–438, 2011.

M. E. Cameron, B. R. Smith-Konter, G. C. Collins, D. A. Patthoff, and R. T. Pappalardo, "Tidal stress modeling of Ganymede: Strike-slip tectonism and Coulomb failure," *Icarus*, vol. 319, pp. 99–120, 2019.

S. C. Solomon, "On volcanism and thermal tectonics on one-plate planets," *Geophysical Research Letters*, vol. 5, no. 6, pp. 461–464, 1978.

G. J. Veeder, A. G. Davies, D. L. Matson, T. V. Johnson, D. A. Williams, and J. Radebaugh, "Io: Heat flow from small volcanic features," *Icarus*, vol. 245, pp. 379 – 410, 2015. [Online]. Available: http://www.sciencedirect.com/science/article/pii/S0019103514004138

F. Marchis, R. Prangé, and J. Christou, "Adaptive optics mapping of Io's volcanism in the thermal IR (3.8 μm)," *Icarus*, vol. 148, no. 2, pp. 384–396, 2000.

K. de Kleer, I. de Pater, A. G. Davies, and M. Ádámkovics, "Near-infrared monitoring of Io and detection of a violent outburst on 29 August 2013," *Icarus*, vol. 242, pp. 352–364, 2014.

I. de Pater, A. G. Davies, M. Ádámkovics, and D. R. Ciardi, "Two new, rare, high-effusion outburst eruptions at Rarog and Heno Paterae on Io," *Icarus*, vol. 242, pp. 365–378, 2014.

G. J. Veeder, A. G. Davies, D. L. Matson, T. V. Johnson, D. A. Williams, and J. Radebaugh, "Io: Volcanic thermal sources and global heat flow," *Icarus*, vol. 219, no. 2, pp. 701 – 722, 2012. [Online]. Available: http://www.sciencedirect.com/science/article/pii/S0019103512001339

J. Spencer, S. Stern, A. Cheng, H. Weaver, D. Reuter, K. Retherford, A. Lunsford, J. Moore, O. Abramov, R. Lopes *et al.*, "Io volcanism seen by New Horizons: A major eruption of the Tvashtar volcano," *Science*, vol. 318, no. 5848, pp. 240–243, 2007.

R. M. Lopes and J. R. Spencer, *Io After Galileo: A New View of Jupiter's Volcanic Moon*. Springer Science & Business Media, 2007.

T. Becker and P. Geissler, "Galileo global color mosaics of io," in *36th Annual Lunar and Planetary Science Conference*, vol. 36, 2005.

J. Rathbun, J. R. Spencer, R. M. Lopes, and R. R. Howell, "Io's active volcanoes during the New Horizons era: Insights from New Horizons imaging," *Icarus*, vol. 231, pp. 261–272, 2014.

P. Geissler, A. McEwen, C. Phillips, L. Keszthelyi, and J. Spencer, "Surface changes on Io during the Galileo mission," *Icarus*, vol. 169, no. 1, pp. 29–64, 2004.

J. Rathbun, J. Spencer, L. Tamppari, T. Martin, L. Barnard, and L. Travis, "Mapping of Io's thermal radiation by the Galileo photopolarimeter–radiometer (PPR) instrument," *Icarus*, vol. 169, no. 1, pp. 127–139, 2004.

A. G. Davies, *Volcanism on Io: A comparison with Earth*. Cambridge University Press, 2007, vol. 7.

P. J. Clark and F. C. Evans, "Distance to nearest neighbor as a measure of spatial relationships in populations," *Ecology*, vol. 35, no. 4, pp. 445–453, 1954.

B. B. Mandelbrot and J. W. Van Ness, "Fractional brownian motions, fractional noises and applications," *SIAM review*, vol. 10, no. 4, pp. 422–437, 1968.

N. Ribe and D. De Valpine, "The global hotspot distribution and instability of D"," *Geophysical research letters*, vol. 21, no. 14, pp. 1507–1510, 1994.

C. L. Johnson and M. A. Richards, "A conceptual model for the relationship between coronae and large-scale mantle dynamics on Venus," *Journal of Geophysical Research: Planets*, vol. 108, no. E6, 2003.

N. Sneeuw, "Global spherical harmonic analysis by least-squares and numerical quadrature methods in historical perspective," *Geophysical Journal International*, vol. 118, no. 3, pp. 707–716, 1994.

G. Schubert, J. Anderson, T. Spohn, and W. McKinnon, "Interior composition, structure and dynamics of the Galilean satellites," *Jupiter: The planet, satellites and magnetosphere*, vol. 1, pp. 281–306, 2004.

M. A. Richards, B. H. Hager, and N. H. Sleep, "Dynamically supported geoid highs over hotspots: Observation and theory," *Journal of Geophysical Research: Solid Earth*, vol. 93, no. B7, pp. 7690–7708, 1988.

E. D. Jackson, "Linear volcanic chains on the Pacific plate," *The Geophysics of the Pacific Ocean Basin and its Margin*, vol. 19, pp. 319–335, 1976.

R. Greenberg and P. Geissler, "Europa's dynamic icy crust," *Meteoritics & Planetary Science*, vol. 37, no. 12, pp. 1685–1710, 2002.

H. Jara Orué, "Rotational Dynamics of Icy Satellites: Tidal response and forced longitudinal librations at the surface of a viscoelastic Europa," 2016.

R. W. Gaskell, S. P. Synnott, A. S. McEwen, and G. G. Schaber, "Large-scale topography of Io: Implications for internal structure and heat transfer," *Geophysical research letters*, vol. 15, no. 6, pp. 581–584, 1988.

W. H. Press, S. A. Teukolsky, W. T. Vetterling, and B. P. Flannery, *Numerical recipes 3rd edition: The art of scientific computing*. Cambridge university press, 2007.

P. J. Tackley, "Convection in Io's asthenosphere: Redistribution of nonuniform tidal heating by mean flows," *Journal of Geophysical Research: Planets*, vol. 106, no. E12, pp. 32 971–32 981, 2001.

A. Rittmann, *Volcanoes and their activity*. Interscience Publishers, 1962.

L. Han-Shou, "Convection generated stress field and intra-plate volcanism," *Tectonophysics*, vol. 65, no. 3-4, pp. 225–244, 1980.

M. Poinelli, "Toward a better Understanding of Europa Crevasses: Application of Linear Elastic Fracture Mechanics to Europa," *TU Delft Repository*, 2017.

J. A. Rathbun, R. M. Lopes, and J. R. Spencer, "The global distribution of active Ionian Volcanoes and implications for tidal heating models," *The Astronomical Journal*, vol. 156, no. 5, p. 207, 2018.

NASA, "NASA Selects 4 Possible Missions to Study Secrets of the Solar System," Feb 2020. [Online]. Available: https://www.nasa.gov/press-release/nasa-selects-four-possible-missions-to-study-the-secrets-of-the-solar-system

A
AUXILIARY FIGURES

A.1. CURVE RECONSTRUCTION

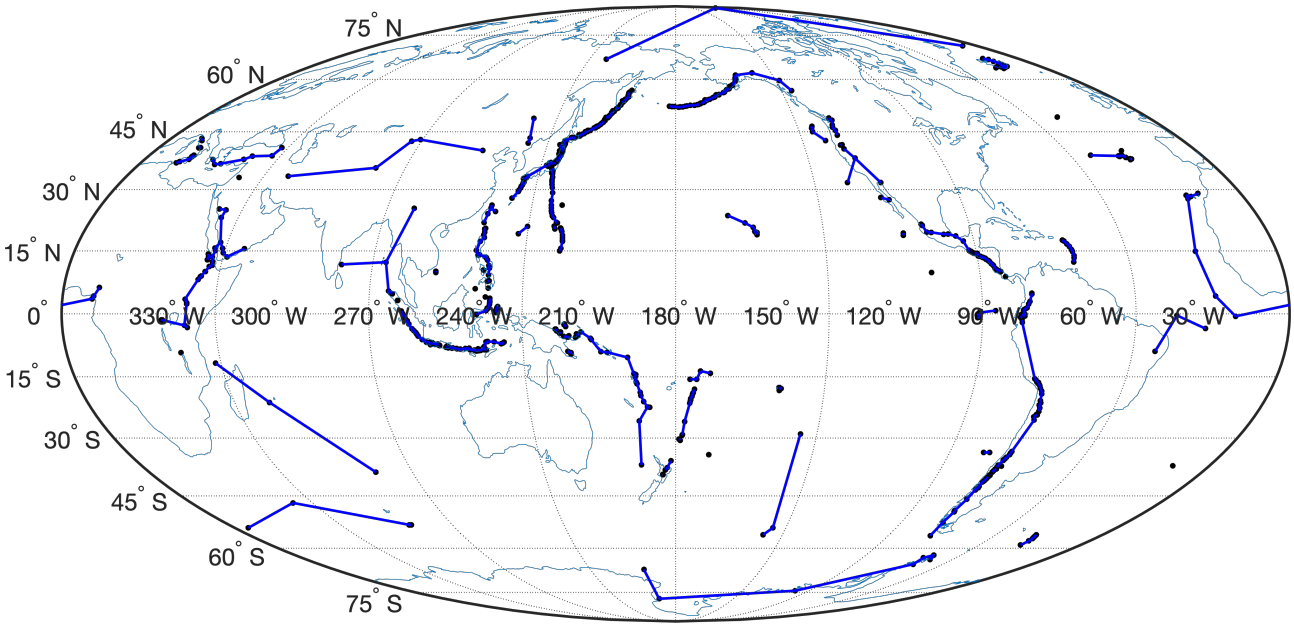

Figure A.1: Mollweide projection of the reconstructed curve for 650 volcanoes on Earth. Locations of volcanoes obtained from the volcanic index from Sigurdsson et al. (2015).

A.2. DIURNAL STRESS

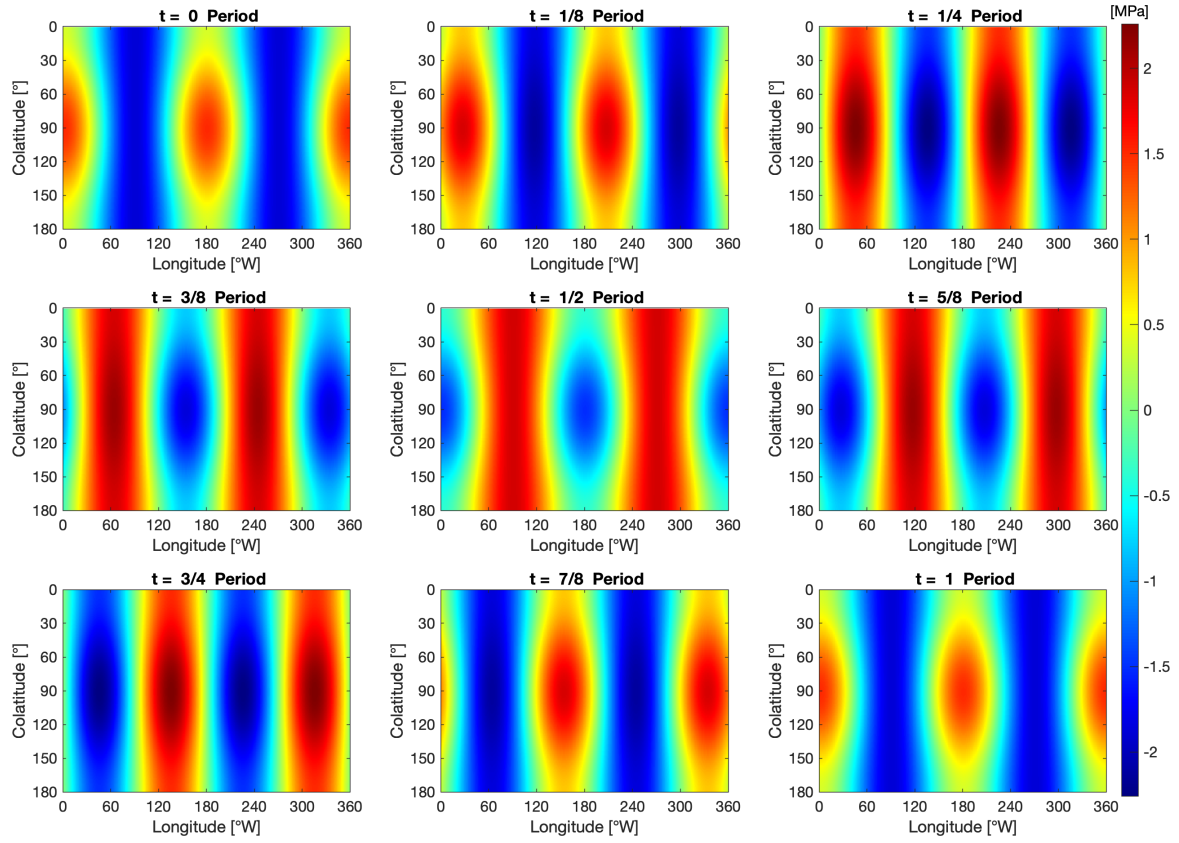

(a)

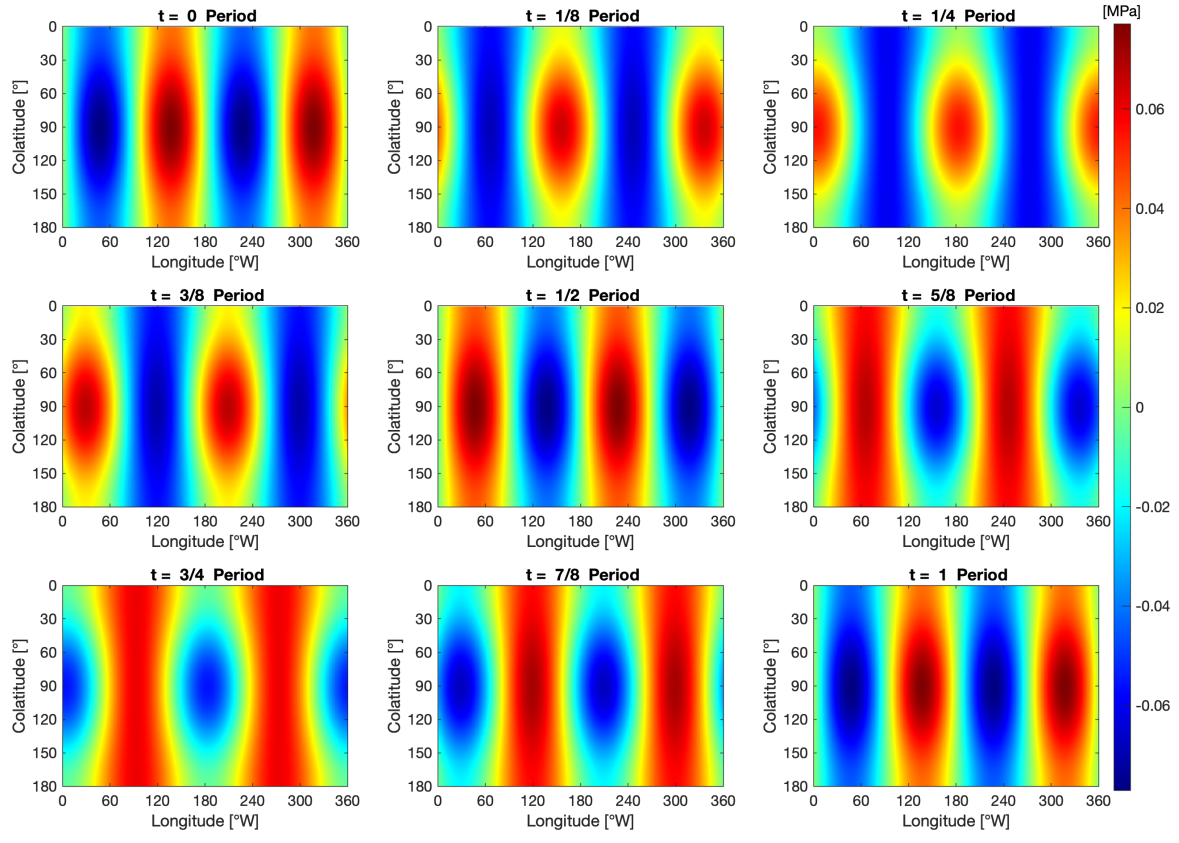

(b)

Figure A.2: The normal stress $\sigma_{\theta\theta}$ at the surface of Io over one orbit. The elastic components (a) and the viscoelastic components (b). Note the significant difference in amplitude.

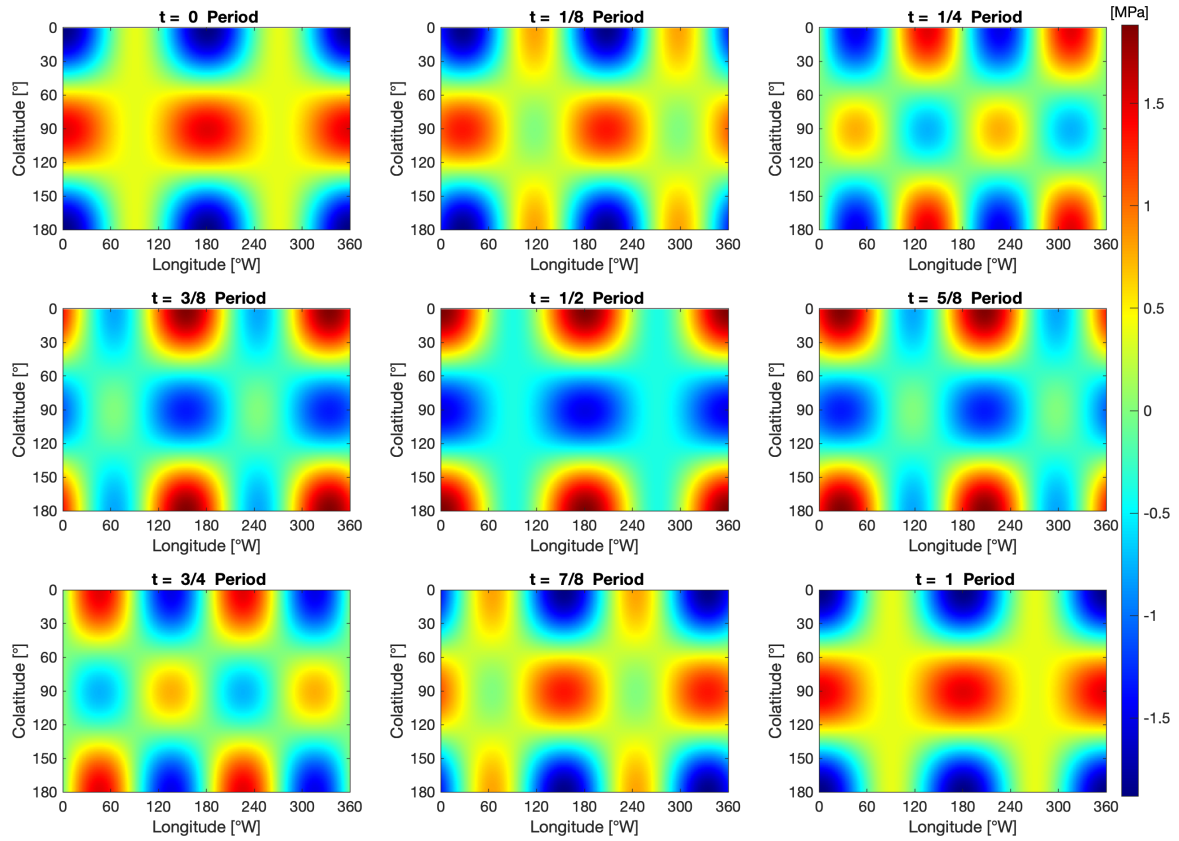

(a)

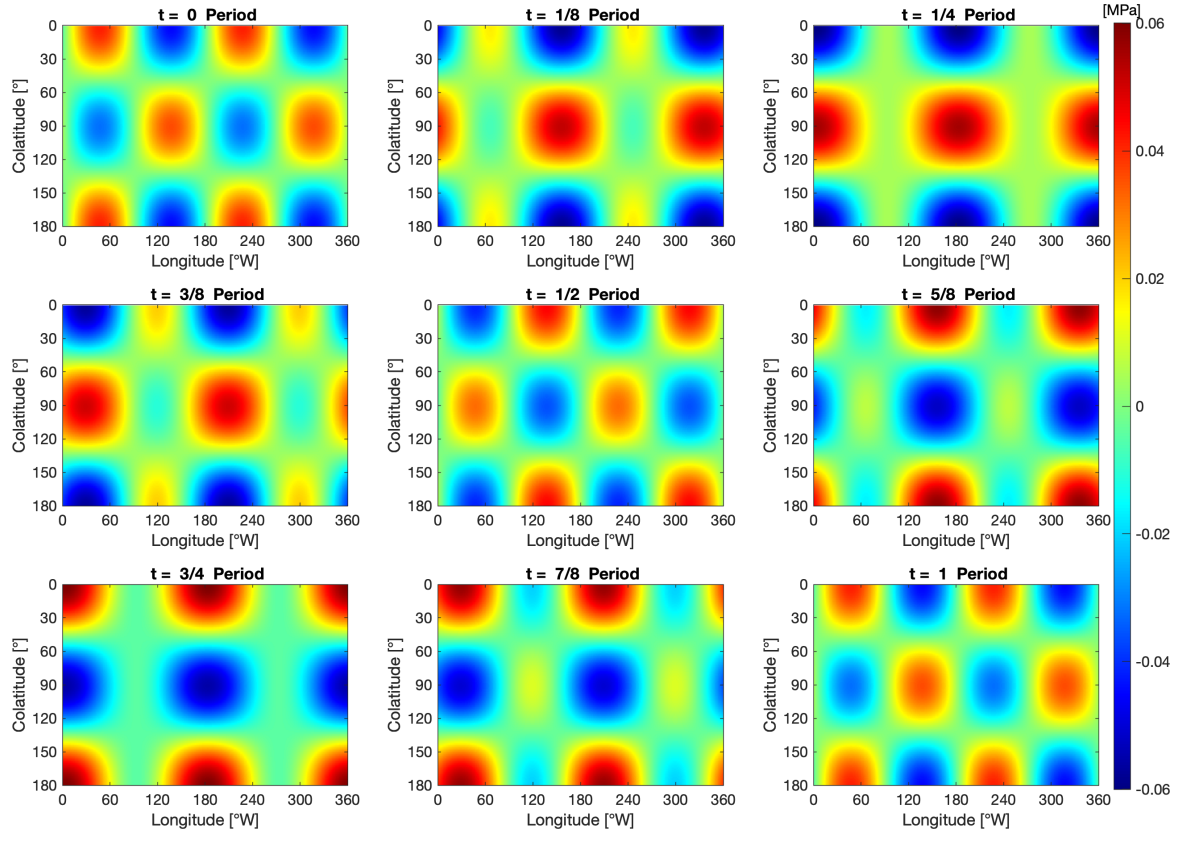

(b)

Figure A.3: The normal stress $\sigma_{\phi\phi}$ at the surface of Io over one orbit. The elastic components (a) and the viscoelastic components (b). Note the significant difference in amplitude.

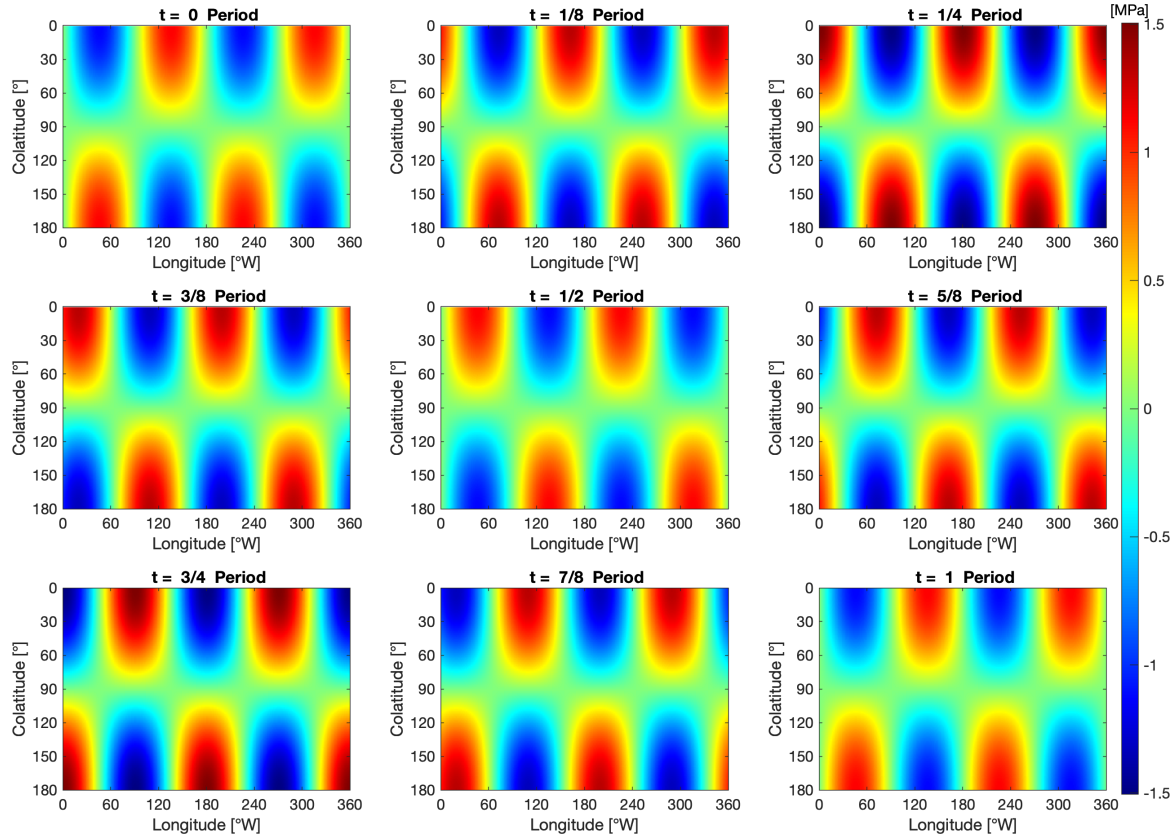

(a)

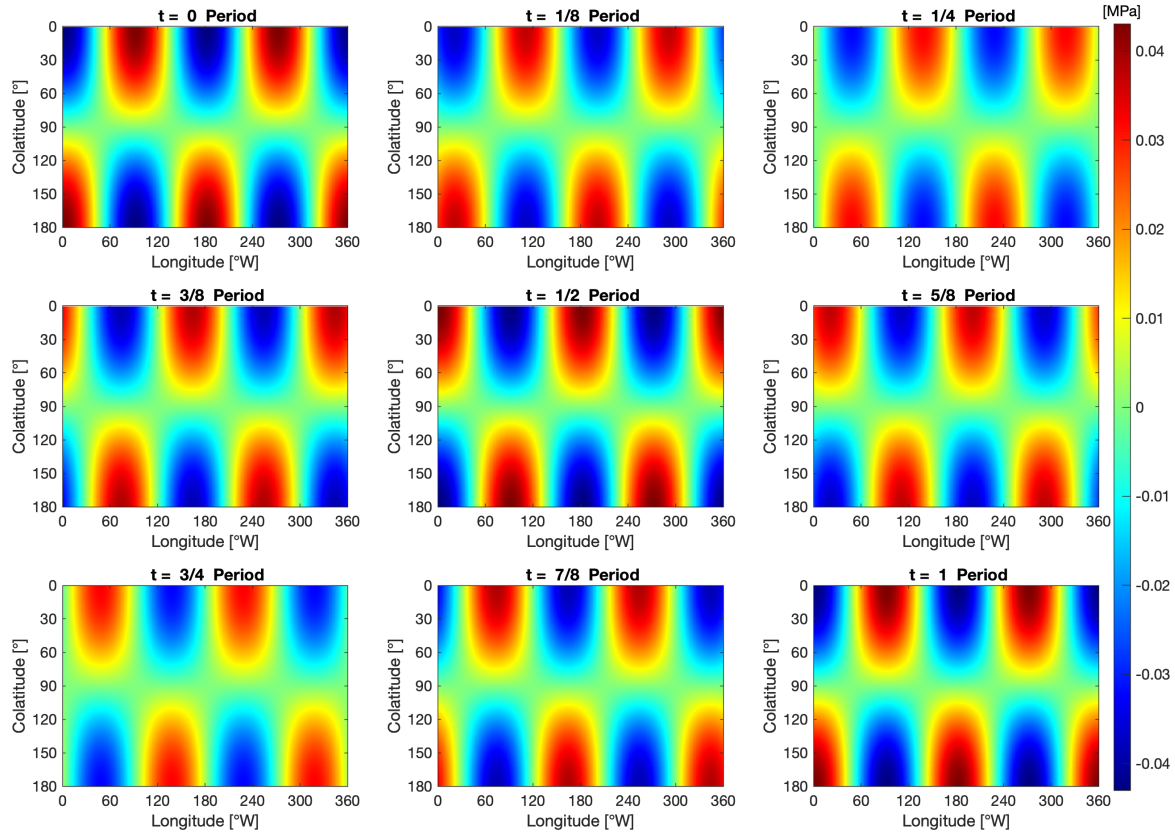

(b)

Figure A.4: The shear stress $\sigma_{\theta\phi}$ at the surface of Io over one orbit. The elastic components (a) and the viscoelastic components (b). Note the significant difference in amplitude.